University of Padova

DEPARTMENT OF PHYSICS AND ASTRONOMY "GALILEO GALILEI"
Master's Course in Astronomy

THE ENVIRONMENT OF MERGING BLACK HOLES AND NEUTRON STARS ACROSS COSMIC TIME

Master's Thesis

Candidate:
Mattia Toffano

Thesis Supervisor:
Prof. Alberto Franceschini

Research Supervisor:
Prof. Michela Mapelli

Academic Year 2017-2018

Contents

Chapter 1

Introduction

Before the first detection of Gravitational Waves (GW) by LIGO in 2015, their existence has been hypothesized and expected by General Relativity theory. The signal detected has been explained as ripples of space-time due to 2 black holes (BH) of masses 36 $M_\odot$ and 29 $M_\odot$ respectively, undergoing a merger at a measured light distance of 410 Mpc (Abbott et al. 2016). After this event, called GW150914 by the date of discovery, other 5 have been detected, involving merging black holes binaries and, for the first time in August 2017, a collision between neutron stars (NS). This last event, called GW170817, has been also the first occasion for astronomers to observe an event both via electromagnetic signal and gravitational waves, definitely opening an era for multi-messenger astrophysics. In just few years, gravitational-wave observations have revolutionized our knowledge about compact objects. Before GW150914 no merging black hole binary has effectively been detected, so with that we had the proof that BHs can merge within a Hubble time. Moreover, with the collision of two neutron stars we know now how heavy elements such as gold and platinum can form in the universe, giving hints on cosmological elements abundances.

1.0.1 Aim and Thesis' Structure

The aim of this work is to study the environment of merging compact objects, in specific black hole-black hole (BHB), black hole-neutron star (NSBH) and double neutron star (DNS) binaries, across cosmic time. We want to analyze properties of binaries' host galaxies in which compact objects form and merge and characteristics of their progenitor stars at different redshifts. The approach we follow is to combine population-synthesis codes for massive stars into a cosmological context by means of a Monte Carlo method. In this way, we generate a huge catalog of compact object binaries for which we can make a statistic of their progenitors' and their hosts' properties at various epochs. In particular, we focus on formation time and metallicity (Z) of progenitors, time at which the merger occurs and the masses of host galaxies when both stars form and merge, finding out if any correlation between these properties exists.

In Chapter 1 we will give an introductory description of the mechanisms which bring compact objects to merge and how they can be detected through gravitational waves; in Chapter 2 we will show how we combined a population-synthesis code with a cosmological simulation to achieve our aim; finally in Chapter 3 we present our results.

1.1 Gravitational Waves detection

In this Chapter we will give a short presentation on how GWs are detected by the LIGO interferometers (Section 1.1) and show which are the astrophysical implications for gravitational

waves discoveries (Section 1.2). Then we will briefly describe massive stars late evolution (Section 1.3), evolution in isolated binaries (Section 1.4) and through dynamical interactions (Section 1.5).

1.1.1 LIGO

The two LIGO detectors are advanced modified Michelson interferometers. A Nd:YAG laser at the frequency of 1064nm of 20W power is pointed towards a beam splitter, which divides the light in 2 directions, orthogonal to each other. In each of these arms there are two mirrors which act as test masses, 4 km far. The beams are then directed back to the beam-splitter and thus towards the detector. The main idea is that a GW transition will alter the length of the two arms by a quantity $\Delta L = h(t)L$, where L is the arm length and $h(t)$ is the GW strain dimensionless amplitude projected onto the detector. Since the different path lengths traveled by laser in the arms, radiation will make interference, observable on the detector (Figure 1.1).

Typical strain values are of the order of $10^{-21} - 10^{-23}$. Compared to the basic Michelson interferometer, many orders of magnitude in sensibility are required to detect GWs. Thanks to a power recycling system and the optical resonant cavity formed by mirrors in the arms, laser's power circulating into them reaches 100kW. Arm's chambers are kept at ultra-high vacuum, around 10^{-12} atm. Moreover, test masses are suspended from the ground by a sophisticated system implemented to minimize any seismic noise. LIGO's structure makes it have blind spots. Incoming GWs which alter arms length of the same amount are invisible to the detector.

The observational frequency range spans from 10 Hz to 10000 Hz, but with a low sensitivity under 100 Hz. With the actual resolution it is possible to detect and successfully split signal from noise for GWs till around $z \sim 0.5$. LIGO will be upgraded soon to reach its design sensitivity in 2020, with improvement on signal detection under 100 Hz and measurable strain till the order of 10^{-23}, which results in an extended observational horizon to higher redshifts, around $z \sim 1$.

Nowadays there are 3 GW detectors: 2 LIGO detectors are in Washington and in Louisiana, while Virgo is in Italy. Another structure, named INDIGO, is planned to be built in India. A major number of detectors sensibly improves sky coverage and enhances data accuracy; in particular, polarization components of GWs can be satisfactorily decoupled.

1.1.2 Detection

According to General Relativity theory (GR), gravitational waves are emitted from objects which have non-null quadrupole of mass momentum. For what concerns this thesis, emission of GWs is expected from the loss of orbital energy during the merger phase of a binary

$$E_{orb} = -\frac{Gm_1m_2}{2l}$$

where l is binary's semi-major axis. From GR, we know that the whole merging process is made of three phases: inspiral, merger, ringdown. During the inspiral phase, the frequency of GWs is connected to the orbital one by

$$f_{GW} = 2f_{orb} = 2\sqrt{\frac{G(m_1 + m_2)}{l^3}};$$

when the binary shrinks, orbital frequency increases and so does the amplitude $h \propto 1/l$ of emitted GWs.

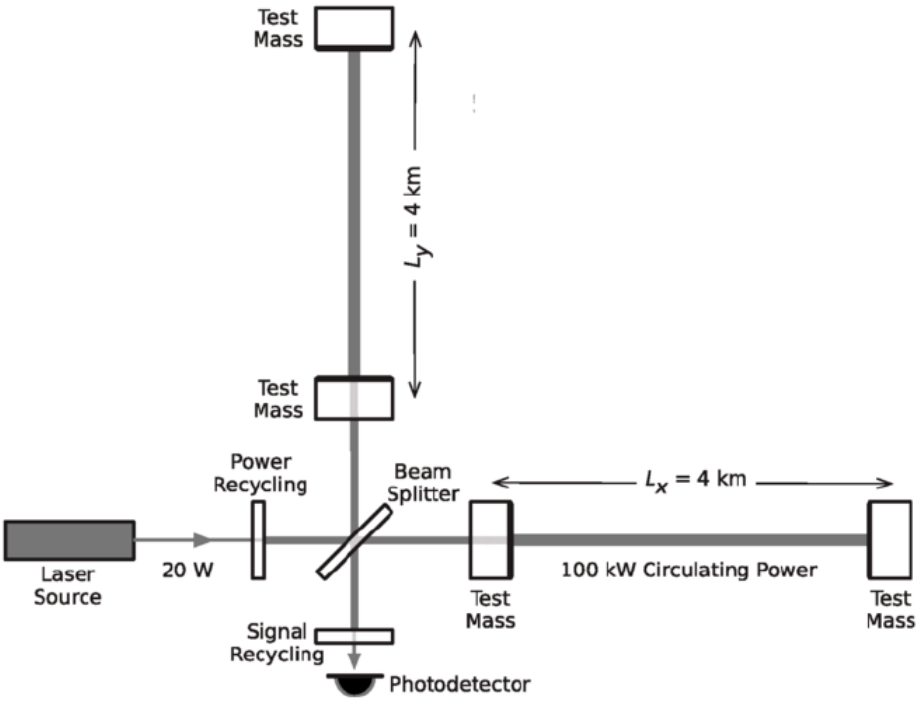

Figure 1.1: Simplified LIGO's structure scheme.

Still during inspiral phase, at lower frequencies, these are correlated with the chirp mass through the relation

$$M_{chirp} = \frac{(m_1 m_2)^{\frac{3}{5}}}{(m_1 + m_2)^{\frac{1}{5}}} = \frac{c^3}{G}\left(\frac{5}{96}\pi^{-8/3} f^{-11/3}\dot{f}\right)^{3/5}$$

where m_1 and m_2 are the masses of the two compact objects in the binary, f and $\dot{f}$ the observed frequencies and its time derivative. Similarly, the total mass is related to the maximum frequency during the merger phase:

$$M_{tot} = m_1 + m_2 = \frac{2c^3}{6^{3/2}\pi f_{ISCO}}$$

where f_{ISCO} is the frequency at the Inner Stable Circular Orbit.

During a GW event, with LIGO we measure signal's frequency and its amplitude h in function of time. h is a dimensionless quantity correlated with both chirp mass and frequency $h \propto M_{chirp}^{5/3} f^{2/3}$ and defined as $h = 2\Delta L/L$, where L is the lenght of LIGO's arms. Reproducing the signal with Post-Newtonian and Numerical Relativity models allows us to infer the quantities M_{chirp} and M_{tot} mentioned above, thus the masses of the two compact objects m_1 and m_2; as example, the model used for GW150914 is shown in Figure 1.2 while signal detected for the same event in Figure 1.3. It is worth mentioning that the frequency we measure is redshifted, so scaled by a factor $(1 + z)$, where z is the cosmological redshift. We cannot directly measure redshift from a GW event without electromagnetic counterpart but we can extrapolate it by means of cosmological models. Indeed, the amplitude is inversely proportional to the luminosity distance of the binary $h \propto 1/D(z)$. So we can directly derive $D(z)$ and use cosmological models to infer z. For GW150914, the ΛCDM model has

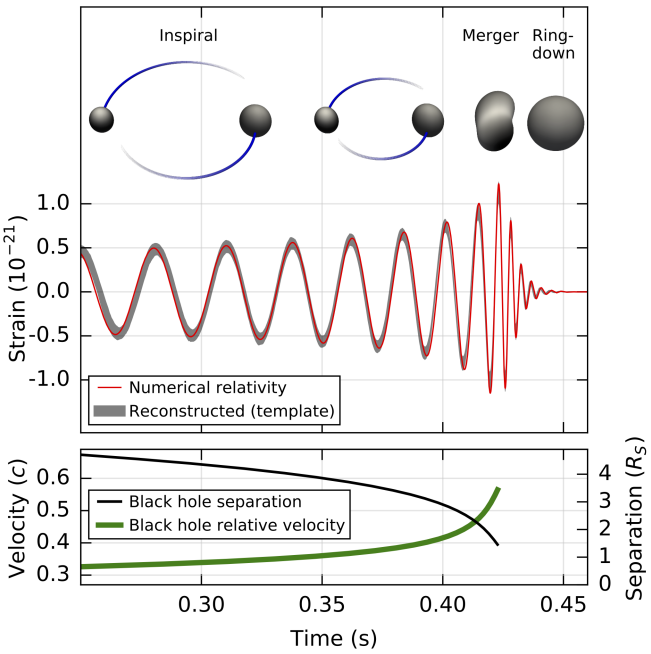

Figure 1.2: *Above*: Estimated theoretical strain amplitude, given by numerical relativity, for the event GW150914. *Below*: estimation of rotational velocity of binary members, measured in fraction of the speed of light c, and their separation, expressed as multiples of Schwarzschild radius, for event GW150914.

been used, with cosmological parameters' values constrained by Planck mission (Abbott et al. 2016).

1.2 Astrophysical Implications

Many implications can be derived already from few detections of merging BHB and DNS binaries.

1.2.1 Black Holes

Mass and Progenitors' Metallicity

For the *No-Hair Theorem* a BH is completely characterized by 3 quantities: mass, spin and charge. We see that the mass range for BHs in binaries is from ~ 5 $M_\odot$ to ~ 40 $M_\odot$ while after-merger remnant masses are in range $\sim 20 - 70$ $M_\odot$. Before the first GW detection the only way to measure the mass of a stellar BH was to make a dynamical mass measurement in a X-ray binary. Masses of BHs obtained in this way are always in range $\sim 5 - 20$ $M_\odot$, never above (Figure 1.4). A question may be why we do not see black holes with masses > 20 $M_\odot$ in an X-ray binary. If BHs detected by LIGO are of stellar origin, it could be due to an observational bias (Abbott et al. 2017). Indeed, GW170608 is the lightest BHB binary detected through GWs and its components' masses are comparable with ones observed via electromagnetic radiation for BH-star binaries. Other authors proposed various explanations for such issue: BHs detected by means of GWs could be primordial ones (e.g. Bird et al. 2016; Carr et al. 2016; Inomata et al. 2016; Magee & Hanna 2017); or they come from previous

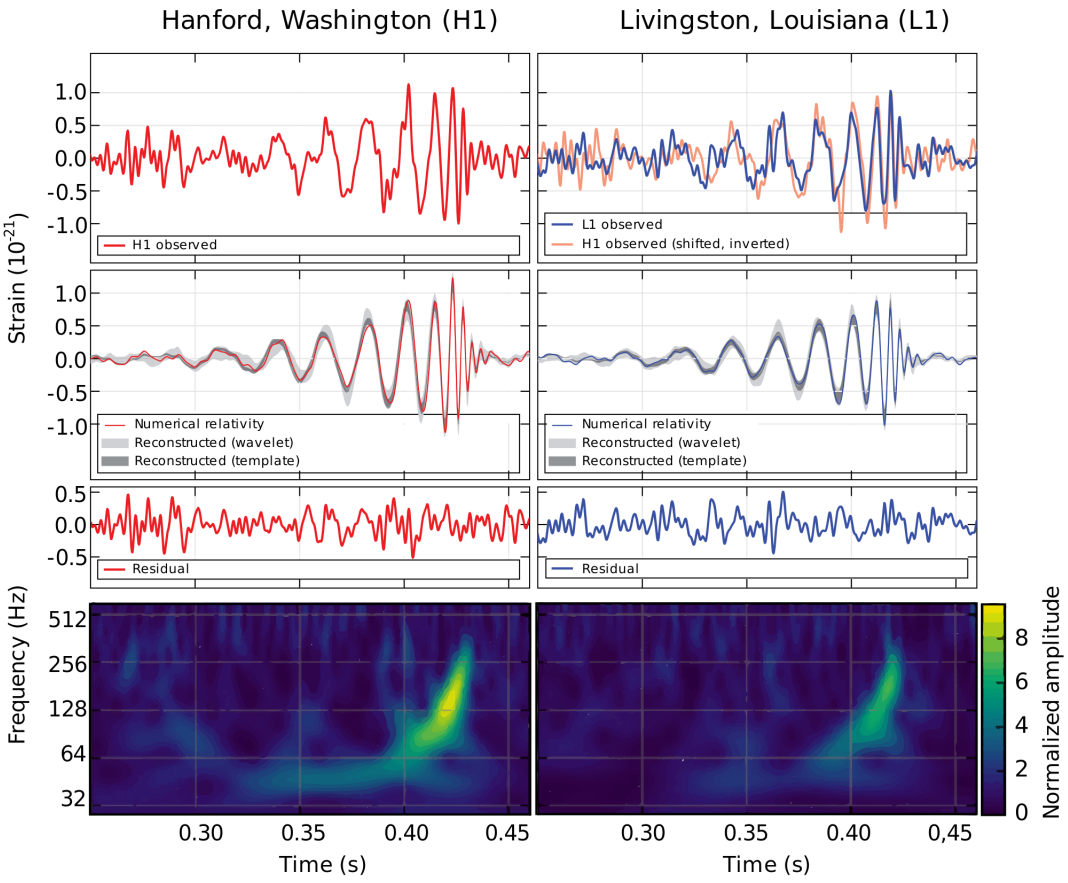

Figure 1.3: *Top*: Signal measured by the LIGO detectors in Washington and Louisiana for the event GW150914; *Middle*: Reconstruction of the signal with a model, with relative residuals; *Bottom*: Frequencies detected and normalized amplitude

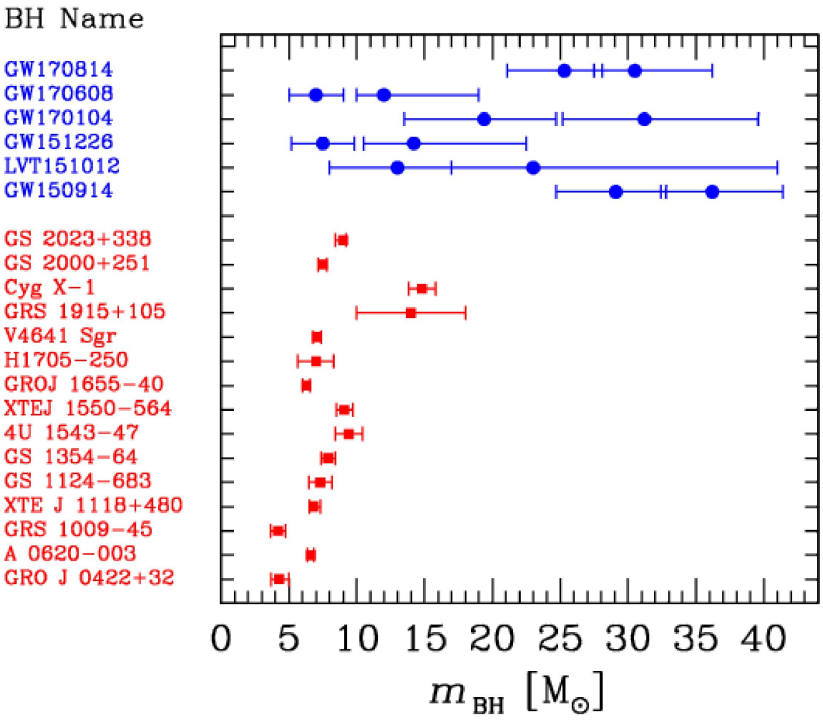

Figure 1.4: Collection of estimated masses of BH in binaries with uncertainties. Blue circles stand for BHs involved in a GW event while red squares represent BHs in a X-ray binary. The gap of masses measured by GWs detection and X-ray spectroscopy is clear.

mergers (Gerosa & Berti 2017); or even GWs emitted from such BHs might be lensed across their path till us (Broadhurst et al. 2018). This topic is still matter of debate.

Recent models involving new more accurate theories on mass loss due to stellar winds and on final phases of star life have been validated by GW150914 detection. Using such models, we have seen that BHs involved in the event GW150914 must have formed in a low-metallicity environment, certainly below $Z_\odot/2$ and likely below $Z_\odot/4$ (Belczynski et al. 2010a; Mapelli et al. 2013; Spera et al. 2015). With increasing redshift we will see more low-metallicity progenitors, thus we expect to find BHs with masses above 10 $M_\odot$ more frequently when LIGO will reach full design sensitivity in 2020.

Spin

The spin of a BH is defined as

$$\vec{S} = \frac{\vec{J}c}{GM^2},$$

where $\vec{J}$ is the angular momentum of the rotating BH with mass M, $G = 6.67\times10^{11}$ Nm^2 kg^{-2} is the universal gravitational constant and $c = 2.99 \times 10^8$ m s^{-1} is the speed of light. For construction, $S \in [0, 1]$. Currently, LIGO can measure only the value of the effective spin χ_{eff} given by

$$\chi_{eff} = \frac{c}{G(m_1 + m_2)} \left(\frac{\vec{S}_1}{m_1} + \frac{\vec{S}_2}{m_2} \right) \cdot \frac{\vec{L}}{|\vec{L}|} = \frac{(m_1\chi_1 + m_2\chi_2)}{m_1 + m_2}$$

where $\vec{S}_1$ and $\vec{S}_2$ are spin angular momentum of BHs, χ_1 and χ_2 their dimensionless projections and $\vec{L}$ the orbital angular momentum of the binary. By definition $-1 < \chi_{eff} < 1$; positive values mean aligned spins while negative ones mean misalignment with respect to the binary angular momentum. Farr et al. (2016) found that the way how BHs formed should be strictly connected with their spins. A scenario in which BHs form in an isolated binary will result in a preference for aligned spins and small natal kicks (although the details of spin evolution especially during a supernova (SN) are still very uncertain). On the other hand, if a binary formed due to dynamical interaction, BHs' spins will be either low or high and mostly misaligned. Another possibility is that these BHs are of primordial origin; in this case spins will be low and misaligned. Farr et al. (2016) foresaw that around 10 more detections will be sufficient to put constraints on spins strong enough to determine the formation channel, which will be achieved within a couple of years following present detection rate by LIGO.

Merger Rate

An estimation of the merger rate for BHB mergers has been inferred since the first detection. Assuming that all BHB binaries have the same masses and spins of GW150914, that the BHB merger rate is constant in the cosmological comoving frame and taking into account the uncertainties in the astrophysical detections and LIGO's actual observational range ($z \lesssim 0.5$), Abbott et al. (2016) constrained the merger rate for BHB in a conservative range of $2 - 600$ Gpc^{-3}yr^{-1}. Extreme models which predicted rates lower than 1 Gpc^{-3}yr^{-1} have thus been excluded.

It is worth mentioning that BH progenitors could have had birth in the early universe and have merged at low redshift as well as formed at low redshift and merged after a short time. The elapsed time between the moment when progenitors formed and they finally merge is called delay time. From just the first detection is not possible to put constraints on this quantity (Abbott et al. 2016). We will examine this feature in the present work.

1.2.2 Neutron Stars

Mass

Other implications are related to neutron stars. Firstly, we have seen that they merge, but we do not know if a remnant exists or if both stars get destroyed during the process. Secondly, as shown in Figure 1.5, we see a gap between masses of known NSs and BHs. Surely the gap is related to the mechanism that forms the compact object. Standing on known stellar evolution, a star in which the electron-degenerated Helium core exceeds the Chandrasekhar limit, estimated to be 1.44 $M_\odot$, cannot sustain hydrodynamical equilibrium against gravity and will undergo a collapse with probable subsequent SN explosion. This may leave a NS remnant with a mass of $\sim 1 - 2$ $M_\odot$. The collapse can directly lead to a BH if the core is heavier than the Oppenheimer-Volkoff limit, which has been estimated around 3 $M_\odot$. Thus, BHs might form with masses of $3 - 4$ $M_\odot$ even if we do not observe them. The study of supernovae and collapse mechanisms requires an accurate knowledge of the Equation of State (EOS) of massive stars interiors, which nowadays is still incomplete. It may be that BHs with those masses cannot form; moreover, the relation "initial mass - remnant mass" may not be even monotonic and thus we might see neutron stars as remnants above a certain initial mass limit (Woosley et al. 2002).

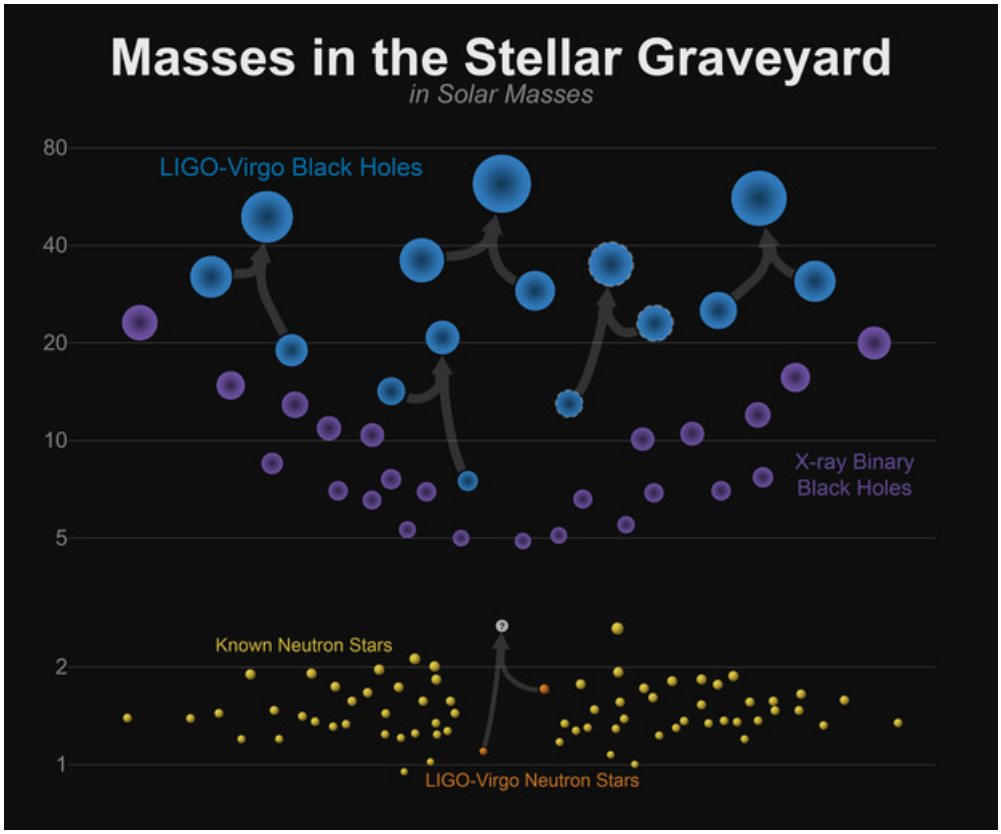

Figure 1.5: The graphic shows masses of BHs detected by means of gravitational waves in *blue* and X-ray spectroscopy in *violet*; neutron star masses measured by electromagnetic signal are in *yellow* while by gravitational waves (GW170817) in *orange*. The eventual remnant of GW170817 is labeled with a question mark.

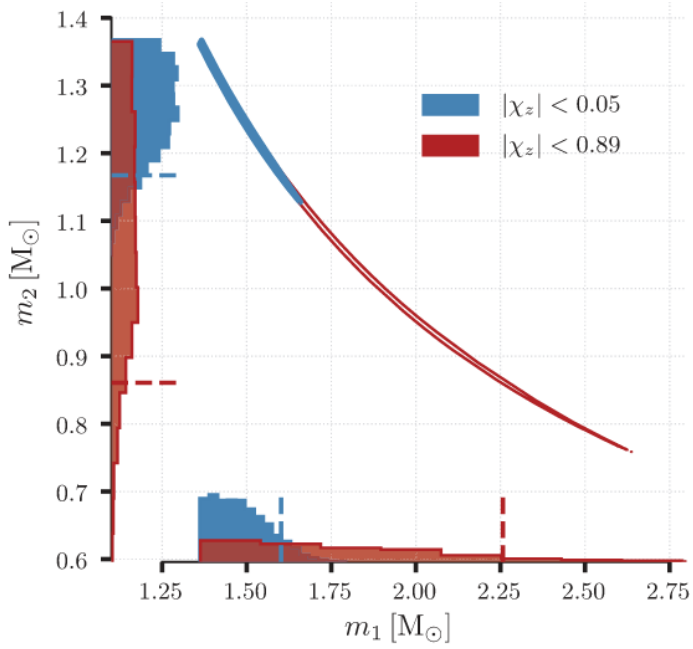

Figure 1.6: Two-dimensional distribution for members' masses m_1 and m_2 in source rest frame. In *blue* the low-spin scenario while in *red* the high-spin one. The shape of this distribution is determined by a line of constant M_{chirp} showed above, whose width is due to M_{chirp} uncertainties. Dashed lines enclose 90% probability away from a equal mass of 1.36 M$_\odot$ for both NSs.

Spin

The chirp mass is well constrained by the observed signal but due to the degeneracy between the mass ratio $q = m_1/m_2$ (where m_1 and m_2 are the masses of NSs) and spins of the NSs, estimates on members' masses depend on the assumption on admissible spin values. We show in Figure 1.6 how m_1 and m_2 vary with the spin value assumptions for GW170817 (Abbott et al. 2017). They hypothesized a first case in which spins are low and a second one in which spins are high, recovering q and subsequently individual components' masses. The obtained values are consistent with all known ones for NSs in a binary system.

Merger Rate

Since GW170817 is the only detection of a DNS merging binary, the merger rate of DNSs can be estimated with a large uncertainty. Abbott et al. (2017) found $R = 1540^{+3200}_{-1220}$ Gpc^{-3}yr^{-1}. From this, they estimated that the stochastic background of GWs produced by DNS mergers should be comparable in magnitude with the stochastic background produced by BHB merging binaries.

1.3 Massive Stars Late Evolution

Generally speaking, a star is considered massive if its mass is $\gtrsim 8$ times the mass of our Sun. We say that a star leaves the main sequence (MS) when its core stops burning Hydrogen. The time that a star spends on the MS phase is inversely proportional to its mass (Figure 1.7) so massive star lifespan will be much shorter compared to e.g. solar ones. Massive stars

Mass/M_{Sun}	Luminosity/L_{Sun}	Effective Temperature (K)	Radius/R_{Sun}	Main sequence lifespan (yrs)
0.10	3×10^{-3}	2,900	0.16	2×10^{12}
0.50	0.03	3,800	0.6	2×10^{11}
0.75	0.3	5,000	0.8	3×10^{10}
1.0	1	6,000	1.0	1×10^{10}
1.5	5	7,000	1.4	2×10^{9}
3	60	11,000	2.5	2×10^{8}
5	600	17,000	3.8	7×10^{7}
10	10,000	22,000	5.6	2×10^{7}
15	17,000	28,000	6.8	1×10^{7}
25	80,000	35,000	8.7	7×10^{6}
60	790,000	44,500	15	3.4×10^{6}

Figure 1.7: Some main properties of stars with various masses.

differ from low-mass and intermediate ones in late evolution phases because they reach a sufficiently high temperature ($> 5 \times 10^8$ K) in the Helium core to undergo non-degenerate Carbon ignition. Stars with masses above ~ 11 $M_\odot$ will undergo also heavier elements burning (Oxygen, Neon and Silicon till Iron, which is the element with strongest binding energy). At that point there is no way to keep hydrodynamical equilibrium and a core collapse ends the life of the star.

1.3.1 Stellar Winds

Stellar winds are outflows of matter ejected from the star. They can be induced by radiation pressure on dust present on outer layers of cold stars such as Red Giants or by momentum coupling between photons and ions in massive hot stars' photosphere. Knowledge of how stellar winds work is essential for massive stars' final phases evolution, since they determine the mass of the star in the pre-supernova stage and thus influence the outcome of SN explosion.

De Jager et al. (1988) derived an empirical formula that could fit the average observed mass loss rates for solar-metallicity ($Z_\odot \sim 0.02$) and luminous ($L > 10^3$ $L_\odot$) stars:

$$\log(-\dot{M}) \approx -8.16 + 1.77 \log\left(\frac{L}{L_\odot}\right) - 1.68 \log\left(\frac{T_{eff}}{K}\right)$$

Moreover according to Vink, de Koter et al. (2001) and Nieuwenhuijzen et al. (1990) the mass loss is proportional the metallicity Z of the star

$$\frac{dM}{dt} \propto \left(\frac{Z}{Z_\odot}\right)^\alpha$$

with α is in the range $0.5 - 0.9$. So in general, higher metallicity and higher luminosity (thus mass) imply higher mass loss.

1.3.2 Supernova phase

At the last phases of nuclear burning, massive stars develop a degenerate core made of Carbon or heavier elements, depending on the mass of the star. As the mass of the core approaches Chandrasekhar's limit, the degenerate pressure of relativistic electrons can not

sustain gravitational attraction and hinder the collapse anymore. Electrons get captured by protons in a process which creates neutrons and neutrinos. The core will then be made of degenerated non-relativistic neutrons, which can oppose to collapse. To reach this new equilibrium state, the core has to shrink from a radius of thousand kilometers to few ten in less than a second. The estimated upper limit of gained energy from the gravitational collapse is of the order of 10^{53} erg, while the estimated necessary energy to eject the envelope is just 1% of the gravitational one, around 10^{51} erg. An issue is how this fraction of energy is transferred to the envelope and converted into kinetic energy to trigger the subsequent supernova explosion. The complete mechanism is still uncertain; nowadays the mostly accredited model implies a convective SN engine. According to it, the core induces a shock by bouncing back during the collapse. The energy flux powering the shock is mostly due to neutrinos, which cannot escape given the huge density of the core, despite their extremely small cross section and likelihood of interacting with matter. If neutrinos manage to leak out, the shock will stop and another mechanism is necessary to revive it. This could be done if a layer of the core becomes convectively unstable.

O'Connor & Ott (2011) proposed a parameter useful to establish if a SN has success or not, called compactness and defined as:

$$\xi_M = \frac{M}{R(M)} \frac{1000\text{km}}{\text{M}_\odot}$$

where M is the mass enclosed into a radius $R(M)$. Usually compactness is defined for $M = 2.5$ $\text{M}_\odot$. Through simulations O'Connor & Ott (2011) found that a higher value for $\xi_{2.5}$ result into a shorter time to form a BH thus a star will likely collapse into it without SN explosion, that results into a minor likelihood for a star in binary to disrupt the latter. This single parameter is not sufficient to describe satisfactorily the SN mechanism yet; for example Ertl et al. (2016) suggest a new 2 parameter criterion based on the central entropy of the star.

1.3.3 Remnants

Not all SNe give birth to a stellar remnant. If the explosion is powerful enough to destroy completely the star, all the matter including the core will be disrupted and ejected away. Which type of remnant we will have after the SN phase depends on the SN process and on the properties of the progenitor star. Stars with masses up to 20 $\text{M}_\odot$ are believed to leave a NS remnant. For higher masses, the binding energy of the envelope increases and only a weak explosion could be triggered. In this case the ejected material can fall back onto the proto-neutron star and if by accretion its mass exceeds the Oppenheimer-Volkoff limit, it will subsequently collapse into a BH. If mass loss due to stellar winds is not strong enough and a Carbon-Oxygen core with mass $\gtrsim 8$ $\text{M}_\odot$ is left prior core collapse, an explosion may not be even triggered and we may have a direct collapse into a BH. As said above, we have to take into account that the relation between pre-SN mass and remnant mass may be non-monotonic, so we may have NS remnants even for certain masses above 20 $\text{M}_\odot$ (Figure 1.8).

Usually a supernova explosion induces a natal kick to the new-born compact object. It is known that NSs are one of the fastest moving objects on the sky, with a proper velocity ~ 400 km s^{-1}, but the origin of this natal kick is still matter of debate. A valid hypothesis is that during the supernova phase an asymmetry in the explosion mechanism may form, resulting into a momentum transfer received by the remnant towards one preferred direction; why this asymmetry occurs is unknown.

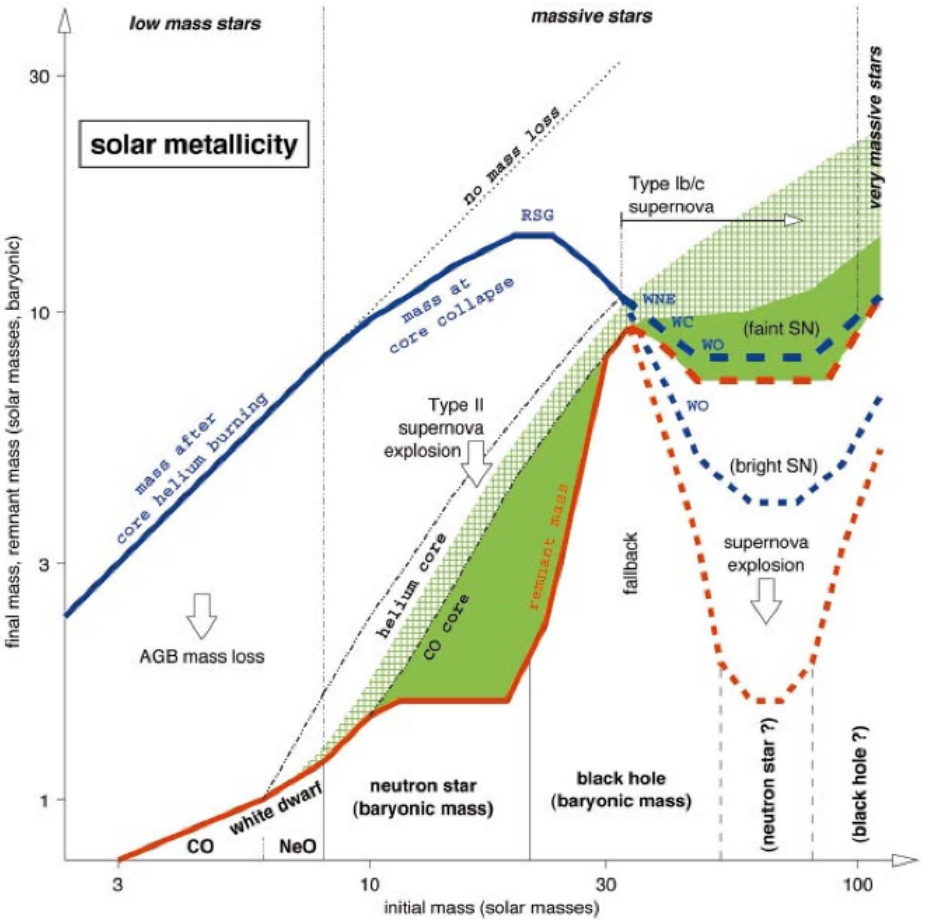

Figure 1.8: Initial-final mass relation of SN phase for stars with solar metallicity. The *blue* line shows stellar mass after He burning while the *red* line indicates the mass of the remnant. The *green* regions show the amount of mass ejected previously processed by nuclear burning. The *dashed* lines show the uncertainty on mass loss rates.

1.3.4 Other relevant mechanisms in pre-SN phase

Strong surface magnetic fields can overcome stellar winds by magnetic confinement; since they are present in 10% of hot stars, they cannot be neglected but are not included in the codes for compact object formation yet, because of heavy computational resource demand.

Rotation also affects massive stars evolution. It increases the luminosity of the star, but at the same time it induces chemical mixing, with the outcome of creating a larger Helium/Carbon-Oxygen core, which will affect the future collapse.

Even if some phases are still matter of debate, evolution of massive stars at solar metallicity can be generically outlined as:

- 8 $M_\odot < M <$ 15 $M_\odot$: MS (type O/B) $\longrightarrow$ RSG $\longrightarrow$ SN II
- 15 $M_\odot < M <$ 25 $M_\odot$: MS (type O) $\longrightarrow$ BSG $\longrightarrow$ RSG $\longrightarrow$ SN II
- 25 $M_\odot < M <$ 40 $M_\odot$ MS (type O) $\longrightarrow$ BSG $\longrightarrow$ RSG $\longrightarrow$ WR $\longrightarrow$ SN Ib
- $M >$ 40 $M_\odot$: MS (type O) $\longrightarrow$ BSG $\longrightarrow$ LBV $\longrightarrow$ WR $\longrightarrow$ SN Ib/c

where RSG, BSG, WR and LBV mean *Red SuperGiant, Blue SuperGiant, Wolf-Rayet* and *Luminous Blue Variable* respectively.

1.4 Evolution in Isolated Binaries

The fate of a star can completely change if it evolves in a binary with another object. Processes of matter exchange can occur, modifying the stellar mass, which we know to be a fundamental parameter in the pre-SN phase. Only if the binary is detached, so the two stars are far enough not to influence each other, they can evolve on their own and likely become a BH binary at the end. Stars can have co-evolved in binary since their birth or they could have had birth separately and joined later due to gravitational attraction. In this Section we will describe evolution for those systems which are not influenced by other bodies' presence, named isolated binaries.

1.4.1 Roche Lobe Overflow

To define the Roche lobe we have to use the restricted three body problem, in which M_1 and M_2 are the masses of our stars and the third mass, negligible, is the one of the test particle. In this case the effective potential is given by the sum of gravitational plus the centrifugal one

$$\Phi(\mathbf{r}) = -\frac{GM_1}{\mathbf{r}-\mathbf{r_1}} - \frac{GM_2}{\mathbf{r}-\mathbf{r_2}} - \frac{1}{2}(\boldsymbol{\omega}\times\mathbf{r})^2$$

in polar coordinates, where $\mathbf{r}$, $\mathbf{r_1}$, $\mathbf{r_2}$ are radius vector from M_1, M_2 and the test particle to the system center of mass and $\boldsymbol{\omega}$ is the centrifugal velocity.

The effective potential $\Phi(\mathbf{r})$ has null value in 5 points, named Lagrangian points, as visible in the Figure 1.9. The Roche lobe is defined as the maximum equipotential surface around the star within which the matter is still bound to it. The lobes of the two stars are connected by the point L_1, so matter that is present on that equipotential surface will indefinitely move from a star to another. So if a star enlarges enough to fill its Roche lobe up, it will start transferring mass to the partner. This mass transfer will obviously alter both star masses and thus the mass of the final remnant but also the orbital properties of the binary. Indeed,

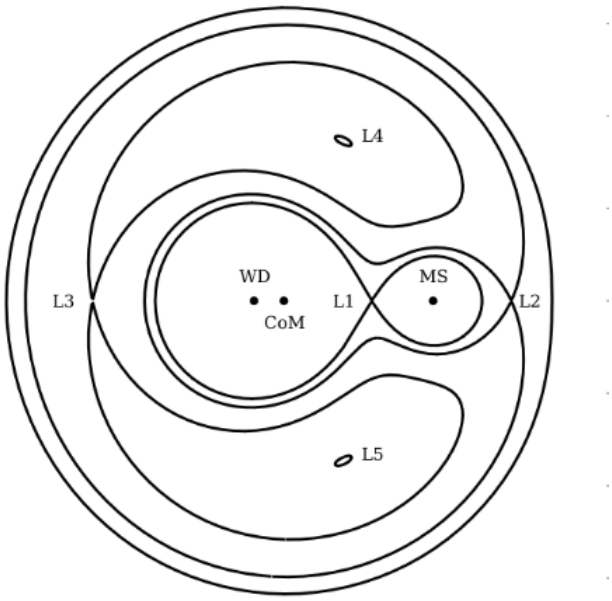

Figure 1.9: Roche equipotential level lines for a generic binary. CoM is the center of mass of the system. Lagrangian points are named L_1, L_2, L_3, L_4 and L_5.

the separation between stars Δa is connected with their mass ratio $q = M_1/M_2$ according to the equation

$$\Delta a = \frac{2(q+1)^3}{q^3}(q-1)\Delta q$$

Usually we use ζ parameters to determine if the mechanism is self-sustained:

$$\zeta_{ad} = \left(\frac{d\ln(R_D)}{d\ln(M_D)}\right)_{ad}$$

$$\zeta_{th} = \left(\frac{d\ln(R_D)}{d\ln(M_D)}\right)_{th}$$

$$\zeta_L = \left(\frac{d\ln(r_L, D)}{d\ln(M_D)}\right)$$

where ζ_{ad} is the change in radius of the donor necessary to adiabatically set the star into the new hydrostatic equilibrium, ζ_{th} analogously is the change of donor's radius to adjust into thermal equilibrium, ζ_L is the change of the radius of the Roche lobe of the donor and R_D, M_D, $r_{L,D}$ are radius, mass and Roche lobe radius of the donor star. The mechanism is stable if $\zeta_{ad} > \zeta_{th} > \zeta_L$ and this results into a shrinking of the Roche lobe during the process of mass transfer, which will carry on till $q \sim 1$, so when both objects will have approximately the same mass. In contrast if r_L is unstable, the two stars will finally merge or enter a Common Envelope (CE) phase.

1.4.2 Common Envelope

If the mass transfer process is self-sustained, the accretor will fill its Roche lobe up as well. Matter orbiting around both stars then stops co-rotating the core and exits from Roche

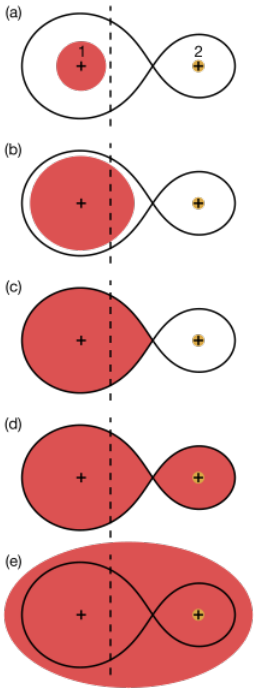

Figure 1.10: Illustration of Roche lobe filling and CE beginning.

lobes. A non-rotating CE forms (Figure 1.10) and the 2 cores begin to spiral-in due to gas drag forces. A part of the orbital energy lost by the 2 stellar cores due to this drag force is converted into heat, making the envelope hotter and thus less bound. This process can lead to the ejection of the envelope from the binary, in which the remnants will be either the 2 naked cores of the previous stars or a naked core and a compact object. Due to the spiral-in effect, their separation will be smaller than before the CE phase has begun, in particular it can likely be shorter than the sum of progenitor stars' radii. The naked core may subsequently collapse into a BH, and if the natal kick does not break the binary, the 2 remaining BHs are close enough to be able to merge into a Hubble time. On the other hand, if the envelope is not ejected away, the objects can merge while they are still in the CE phase. The process is shown in Figure 1.11.

Usually the formalism $\alpha\lambda$ is used to describe CE, even if it is not a complete explanation of the phenomenon. The key idea is that the energy necessary to unbind the envelope comes uniquely from the orbital energy lost by the binary during the spiral-in.

The fraction of energy useful for unbinding the envelope can be expressed as

$$\Delta E = \alpha(E_{b,f} - E_{b,i}) = \alpha \frac{G m_{c1} m_{c2}}{2} \left(\frac{1}{a_f} - \frac{1}{a_i} \right)$$

where $E_{b,f}$ and $E_{b,i}$ are the orbital binding energy after and before the CE phase, α is the parameter that determines the fraction of energy transferred to the envelope, m_{c1} and m_{c2} are the initial masses of the objects and a_f and a_i are the semi-major axis after and before the CE phase.

The binding energy of the envelope is

$$E_{env} = \frac{G}{\lambda} \left(\frac{m_{1,env} m_1}{R_1} + \frac{m_{2,env} m_2}{R_2} \right)$$

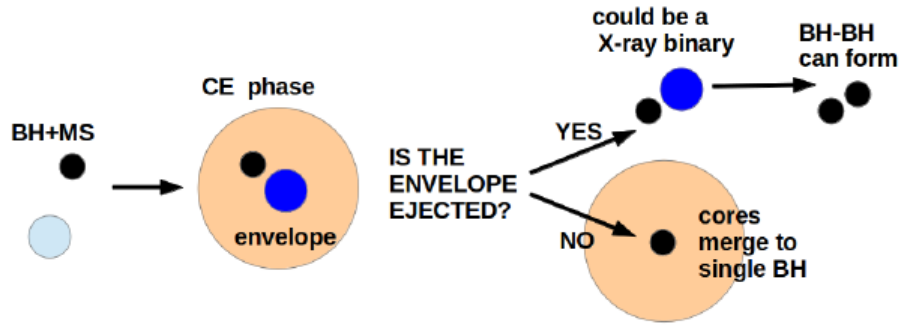

Figure 1.11: Illustration showing the evolution of a BH binary during a CE phase with its possible destinies.

where λ is a parameter which estimates envelope concentration (smaller value means more concentrated envelope), m_1 and m_2 are masses of the members of the binary, $m_{1,env}$ and $m_{2,env}$ are masses of envelope relative to members of the binary and R_1 and R_2 are the radii of members.

By imposing $\Delta E = E_{env}$ we can derive the final semi-major axis when the envelope gets ejected

$$\frac{1}{a_f} = \frac{1}{\alpha\lambda}\frac{2}{m_{c1}m_{c2}}\left(\frac{m_{1,env}m_1}{R_1} + \frac{m_{2,env}m_2}{R_2}\right) + \frac{1}{a_i}$$

If a_f is smaller than the sum of the radii of the 2 cores, the two objects will merge within the CE phase; otherwise the binary survives, with final separation a_f. So smaller values for $\alpha\lambda$ mean smaller separation and higher likelihood of having a merger, and vice versa.

As we have seen, the CE is a critical evolutionary phase in a binary system and a complete description of it is essential for simulations. We have not taken into account that λ will surely vary for different types of stars and along their own evolutionary stages. Moreover, we have observed systems which require $\alpha > 1$, which has no physical meaning; more detailed theory is still needed for a complete explanation of the process.

1.4.3 Alternative Evolution

A chemical homogeneous evolution (CHE) is likely for massive fast-rotating stars, especially for metal-poor ones since stellar winds will not be so efficient in removing spin momentum. The radii of stars following a CHE are much smaller compared to stars which develops a chemical gradient. If the members of the binary are close, their spins will be increased due to tidal synchronization. The consequence is that this type of binaries can avoid CE. Marchant et al. (2016) simulated very close binaries whose members are fast rotating. The results show that if the metallicity is low enough, the binary members can touch each other and form a stable contact binary, which will evolve on a nuclear timescale. The 2 members can thus form a BHB system afterwards, with BH masses around 20 $M_\odot$, which are of the order of estimated masses for GW150914, GW170104 and GW170814 events.

1.5 Dynamical Evolution Scenario

An alternative channel for BH binary formation is the dynamical scenario. The majority of massive stars are in young star clusters. In this dense environment, collisional dynamics has an important role, since a third body may approach the binary and influence its evolution.

1.5.1 Exchanges

If the binary is made of a BH and a low-mass star, a third external BH in the vicinity may replace the star and form a BHB binary. This exchange is quite likely in star clusters and it brings to the formation of more BHB binaries than it can destroy, since the probability of replacing the lightest member of the binary is close to 1 if the third object is more massive than one of the two components, while it is close to 0 if the third element is less massive than both others. Through N-body simulations, Ziosi et al. (2014) showed that in young star clusters more than 90% of BHB binaries formed via dynamical exchange. These differ from isolated binaries for some aspects:

- they are more massive, given the high chances the third body has to interfere with the original members;
- orbits eccentricity is initially very high;
- spins are likely misaligned.

1.5.2 Hardening

Internal energy of a binary can be expressed as:

$$E_{int} = \frac{1}{2}\mu v^2 - \frac{Gm_1m_2}{r}$$

where $\mu = m_1m_2/m_1 + m_2$ is the reduced mass, v the relative speed between members and r their distance.

A third star interacting with the binary can perturb the system gaining kinetic energy at the expenses of the internal one from the binary. This makes binary's orbital major axis shrink. This process can occur a few times and be effective enough to bring the binary into the regime in which GW emission is efficient, leading to a possible merger. We call hard binaries those which have binding internal energy higher than the average kinetic energy of stars in a cluster. Since the time needed by a system to merge is strongly dependent on its semi-major axis $\tau \propto a^4$ (Peters et al. 1964), systems which should have naturally merged on very long timescales could have been brought close enough by hardening effect to merge within a Hubble time.

1.5.3 Ejection

As said, during a three-body encounter, a hard binary exchanges part of its internal energy with the intruder. Consequently the binary recoils with a velocity commonly on the order of few km s^{-1}, but it can reach values around hundreds km s^{-1}. Escape velocity from a globular cluster is around ~ 30 km s^{-1} and even lower for young ones, thus a recoil may likely eject the binary from the star cluster. Even the intruder may be thrown away with the system. In this case the binary stops hardening and the third body will not have chances to enter the binary anymore. Mapelli et al. (2013) and Downing et al. (2011) reported that this process

is very efficient in young clusters: in a timescale of 100 Myr, up to 90% of NSs and 40% of BHs can be thrown out by both SN kicks and dynamical recoil.

Dynamical ejection is a possible explanation for isolated short gamma-ray bursts observed in regions of the sky where there should be no galaxy. In addition to three-body encounters, a binary can be ejected from the host by SN kicks and GW recoils, which can reach velocity around hundreds and thousand km s^{-1}. Ejection by kick or recoil can be avoided in very dense nuclear star clusters, where escape speed values are much higher.

Chapter 2

Methodology

In this Chapter we describe the methodological approach we have used during this thesis work. In particular, we have coupled the results of population-synthesis simulations with the outputs of a cosmological simulation through a Monte Carlo approach.

A straightforward advantage of planting population-synthesis codes' outputs into cosmological simulations is that the properties of the host galaxies can be obtained across cosmic time. This approach requires to use the cosmic star formation rate density and the redshift-dependent mass-metallicity relation (MZR) which are inherent to cosmological simulations. The former is usually well reproduced by most state-of-art cosmological simulations while the MZR is more troublesome.

Following this approach, in this Chapter we describe the population-synthesis code MOBSE and its main features (Section 2.1), we introduce the Illustris project (Section 2.2) and describe how we planted the former into the latter to achieve our goal (Section 2.3).

2.1 Population-Synthesis Codes

A population-synthesis code is a set of analytic formulas with which we reproduce the evolutionary stages of stars' life. The advantages compared to evolutionary codes are the high compatibility of usage and the less-expensive computational power needed, obtaining basically the same outcomes.

The population-synthesis code we use in our work is MOBSE (Massive Objects in Binary Stellar Evolution, Giacobbo et al. 2018; Giacobbo & Mapelli 2018). It is an upgrade of an already-existing code named BSE, made by Hurley et al. (2002), which has been specifically developed to reproduce the evolution of massive stars and of their remnants in a binary system. The upgrade has been necessary since the majority of population-synthesis code (including BSE) did not predict mass above 30 $M_\odot$ for BHs in binaries, while we know that they exist from GW150914. In particular, the main updates of MOBSE have been on stellar winds and mass loss processes, CE phase, SN phase and natal kick of the compact objects, in detail below.

Stellar Winds and Mass Loss

Mass loss due to stellar winds of hot massive stars, like O and B type, Wolf-Rayet and LBV, has been updated with a dependence on the metallicity of the star, with a law $\dot{M} \propto Z^\beta$ where β can assume the values $\beta = 0.85$ if $\Gamma_e < 2/3$, and $\beta = 2.45 - 2.4\Gamma_e$ if $\Gamma_e \geqslant 2/3$ (Γ_e is the electron-scattering Eddington ratio, that is the ratio between stellar luminosity and Eddington one, standing to Vink et al. 2001, Vink & de Koter 2005, Gräfener & Hamann

2008, Chen et al. 2015). The Eddington limit has a fundamental role for very luminous stars, since approaching $\Gamma_e \sim 1$, stellar winds become almost insensitive to the metallicity of the star, drastically enhancing mass loss rate.

Common Envelope Phase

MOBSE uses the $\alpha\lambda$ formalism by Hurley et al. (2002) mentioned above to describe the CE phase. In simulations, lower values of $\alpha\lambda$ mean a more efficient spiral-in mechanism with subsequent higher probability of merging.

The main difference with BSE resides in the treatment of the Hertzsprung Gap. In BSE Hertzsprung-Gap donors entering the CE phase can survive to it; since this results at last into a local BHB merger rate of $R_{BHB} \sim 600 - 800$ Gpc^{-3}yr^{-1}, which is against LIGO's predictions, in MOBSE Hertzsprung-Gap donors are forced to merge.

Supernova phase

Core-collapse SNe follow the rapid and delayed mechanisms described by Fryer et al. (2012). A SN mechanism is said to be rapid if the explosion takes place within 250 ms after the core bounces, while delayed if it occurs later than 0.5 s after the bounce. The main difference between them in the outcome is the number of remnants in the range 2 $M_\odot < M < 5$ $M_\odot$. The rapid core collapse mechanism leads to a gap among the most massive NS (~ 2 $M_\odot$) and the lightest BH (~ 5 $M_\odot$). Dynamical mass measurements of compact objects in X-ray binaries (Özel et al. 2010; Farr et al. 2011) seem to suggest a preference for the rapid SN explosion.

Pulsational pair-instability and pair-instability SNe processes for highly massive stars have been added to the code according to Spera & Mapelli (2017). Because of these instabilities, if the final helium core mass is 65 $M_\odot < M_{\rm He,f} < 135$ $M_\odot$ there will be no remnants due to complete disruption of the star. On the other hand, if $M_{He,f} > 135$ $M_\odot$ the star will likely avoid the pair-instability phase and the outcome will be a direct collapse into a BH.

Natal Kicks

Natal kicks are randomly obtained taking a value from a Maxwellian distribution. For electron-capture SNe, this distribution has a one-dimensional root mean square of $\sigma_{ECSN} = 15$ km s^{-1}, which maximizes the number of merging DNSs standing to Giacobbo & Mapelli (2018). For core-collapse SNe, the one-dimensional root mean square of $\sigma_{CCSN} = 265$ km s^{-1} is used in the fiducial case, according to the study of proper motion of 233 single pulsars by Hobbs et al. (2005). On the other hand, with a value of $\sigma_{CCSN} = 15$ km s^{-1} Mapelli & Giacobbo (2018) found results which are more consistent with LIGO's estimated merger rate for DNSs.

For BHs the kick is scaled by a factor $(1 - f_{fb})$ respect to NSs, where the parameter $f_{fb} \in [0, 1]$ is the amount of fallback on the proto-NS (Fryer et al. 2012, Spera et al. 2015). This depends on the final mass of the carbon-oxygen core and on the final mass of the star at the time of the core collapse beginning.

Other minor updates involve the core radii of massive evolved stars, according to in Hall & Tout (2014) and an extended mass range for zero-age main-sequence star (ZAMS) from $M_{ZAMS} = 5$ $M_\odot$ to $M_{ZAMS} = 150$ $M_\odot$.

2.1.1 MOBSE Results

Metallicity

A crucial parameter for MOBSE is progenitor stars' metallicity. MOBSE has been used to simulate progenitor stars with 12 different metallicities from 0.02 (that is solar metallicity $Z_\odot$) to 0.0002 (1/100 $Z_\odot$). Figure 2.1 shows clearly how we need very low metallicities to describe the high mass of some BHs detected by LIGO. Even for different values for α and λ, only if Z is low enough (at least $Z \lesssim 0.008$), remnant BHs from binaries can reach masses above ~ 30 $M_\odot$. The explanation lies in the new theories adopted for mass loss: stellar winds of metal-poor stars are quenched, so is their mass loss, and they end their life with a larger mass compared to metal-rich counterparts; this can lead to a direct collapse into a BH with mass ~ 30 $M_\odot$ if the final core mass is large enough. Furthermore, the number of merging BHBs is inversely proportional to metallicity: lower Z implies higher number of mergers. At high Z, stellar radii are larger and a major fraction of stars merge before becoming a BHB. Finally, our results show that SN kicks are more efficient on unbinding low-mass (thus high-Z) binaries.

Mass Distribution

Figure 2.2 illustrates how the distribution of total masses of merging BHBs changes with the different input values for α and λ. This shows the importance of a correct and deep representation of CE phase in merging binaries. As mentioned, this formalism is quite rough. Nowadays sophisticated hydrodynamical models are only able to simulate the initial spiral-in phase (Ricker & Taam 2008; Ricker & Taam 2012; Passy et al. 2012; Ohlmann et al. 2016), in which the system evolves on timescale ~ 100 days. When the two members are close enough, the binary evolves on a Kelvin-Helmholtz timescale (10^{3-5} yr) which is computationally prohibitive.

Formation Channels

Giacobbo et al. (2018) discerned between 3 formation channels: systems that stepped into 1 CE phase, systems which passed through multi-CE phases and those which experienced no CE phase. The majority of progenitors of merging BHBs ($\gtrsim 80\%$) underwent just 1 CE phase, while $10 - 20\%$ of them did not experience it. Those binaries which have experienced multiple CE phase are a negligible fraction. More in details, the percentage of systems which underwent no CE phase is 0% for solar-metallicity progenitors but it increases non-monotonically till around 15% with decreasing metallicity. So there is a strong dependence of the probability to enter CE phase with the metallicity of progenitors.

2.2 The Illustris Cosmological Simulation

The Illustris is a state-of-art cosmological simulation of galaxy formation which is focused on reproducing both baryonic and dark matter components of our universe (Vogelsberger et al. 2014). It has a very large cubic box, whose side lenght is 106.5 Mpc (comoving) in order to include the most massive halos. In details, the dark matter resolution is 6.26×10^6 $M_\odot$ while the initial baryonic matter resolution is 1.26×10^6 $M_\odot$. Vogelsberger at al. followed the dynamical evolution of 2×1820^3 elements with a passive evolution of 1820^3 Monte Carlo tracer particles; the total amount of simulated particles reaches 18 billion elements. The model of galaxy formation includes the last theories on stellar evolution, stellar feedback, gas recycling, chemical enrichment, feedback from active galactic nuclei, supermassive black

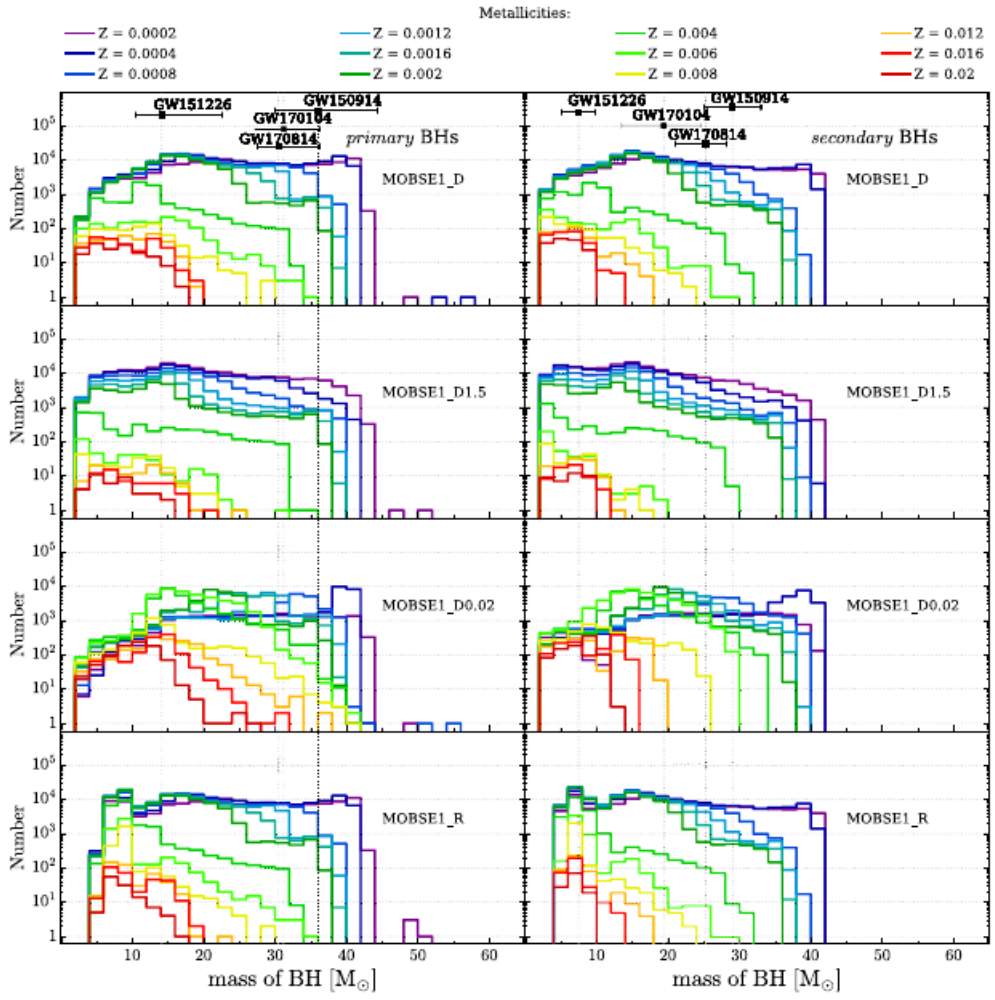

Figure 2.1: Mass distribution for primary (*left column*) and secondary (*right column*) members of BHBs. The colored lines refer to various metallicities from 0.02 to 0.0002, listed above. Vertical lines are the masses of primary and secondary members of GW151226, GW150914, GW170104 and GW170814 estimated by LIGO's scientific collaboration with relative uncertainties at 90% credibility level. The various panels refer to runs for which different values of α and λ have been used, as well as SN mechanism involved (D = delayed, R = rapid).

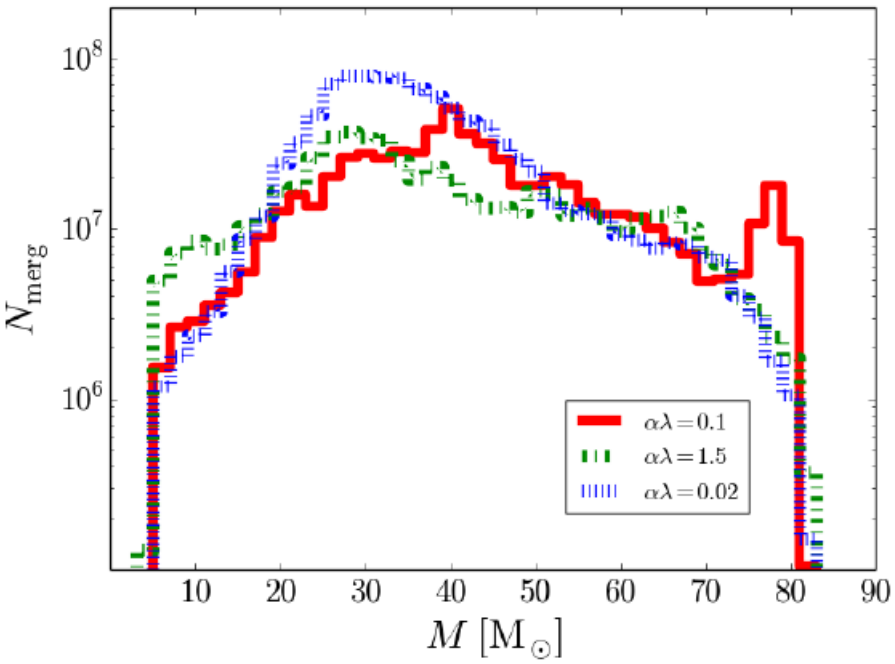

Figure 2.2: Distribution of total masses of merging BHBs within LIGO's instrumental horizon obtained with different combination of α and λ values through MOBSE simulations.

holes growth and primordial and metal-line cooling. At $z = 0$ the outcome consists of a total amount of about 40.000 galaxies of various morphology, from early-type ones to spirals to irregulars. The cosmological parameters that they used for the simulations are the ones estimated by the last Wilkinson Microwave Anisotropy Probe (WMAP-9, Hinshaw et al. 2013):

- total matter density, $\Omega_m = 0.2726$;
- dark-energy density, $\Omega_\Lambda = 0.7274$;
- baryonic matter density, $\Omega_b = 0.0456$;
- density perturbation spectral index, $n_s = 0.963$;
- Hubble constant, $H_0 = 100h$ km s^{-1} (where $h = 0.704$);
- amplitude of the linear power spectrum on the scale of $8h^{-1}$ Mpc, $\sigma_8 = 0.809$.

The aim is to reproduce the evolution of the dark and baryonic matter components of our universe since the first phases after the Big Bang: the simulation begins at $z = 46.77$ which corresponds to an age of the universe ~ 54 Myr. Such large box allows to statistically study the properties of the universe on large scales, standing to the Cosmological Principle of homogeneity and isotropy on such scales. Due to resolution limitations, galaxies with stellar mass below $\sim 10^9$ M$_\odot$ are essentially under-resolved, since they consist in $\lesssim 1000$ particles; this affects the estimation of the cosmic merger rate. The ideal scenario is to have a high-resolution cosmological box able to resolve dwarf galaxies as large as the instrumental horizon of GW detectors. Nowadays this is computationally not possible, so high-resolution simulations have typically small boxes while larger ones, necessary to satisfy the Cosmological

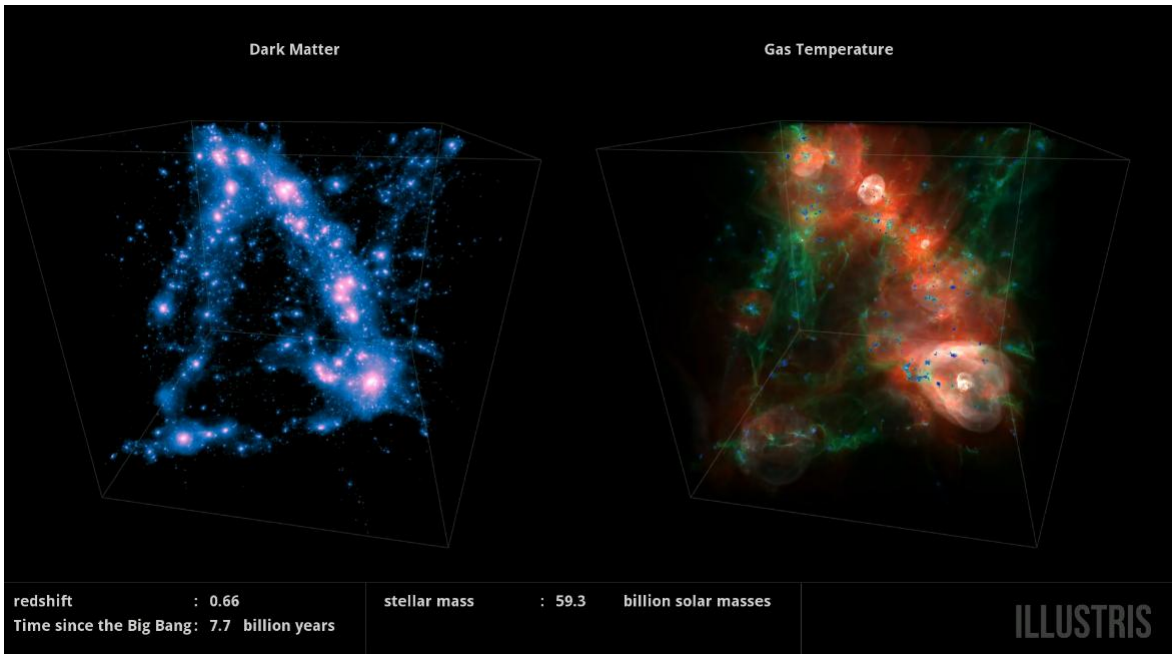

Figure 2.3: Snapshot of the Illustris simulation at redshift $z = 0.66$. *Left*: simulation of the dark matter component; *right*: simulation of baryonic matter. Brighter colors mean higher values for dark matter density and gas temperature. The whole animation is visible at `http://www.illustris-project.org/movies/illustris_movie_cube_sub_frame.mp4`.

Principle, are not able to resolve dwarf galaxies. Thus a complementary approach would be flanking Illustris with a smaller-box higher-resolution simulation in order to adequately resolve galaxies with masses $\lesssim 10^8$ $M_\odot$.

In particular, the main achievements which concern our work are the cosmic merger rate and the intrinsic MZR. The cosmic Star Formation Rate (SFR) agrees with observational data by construction. In particular, a good agreement is maintained till $z \sim 10$, even if a slightly higher formation rate at $z \lesssim 0.3$ is obtained for galaxies with stellar mass around $10^{10-10.5}$ $M_\odot$ with respect to the observed one (Madau & Dickinson 2014). Beyond $z \sim 8$ the model agrees with best observational-data fits by Oesch et al. (2013).

Moreover, physical models included in the Illustris produce a mass-metallicity relation (Genel et al. 2014; Genel 2016), although it strays from the one obtained by observational data. In particular, it doesn't show the turnover at stellar masses higher than $\sim 10^{10}$ $M_\odot$ and the slope is slightly steeper at low metallicities.

2.3 Planting MOBSE into the Illustris simulation

The first step of our work consists in downloading Illustris data from the official website `http://www.illustris-project.org/`. We choose each snapshot from $z = 0$ to $z \sim 16$ (for a total of 108 snapshots). In each one, we find Illustris stellar particles with information on their initial mass, formation time and metallicity. Initially, we store the properties of each Illustris stellar particle: initial mass M_{Ill}, metallicity Z_{Ill} and formation redshift z_{Ill}. We do the same for each compact object simulated to merge within a Hubble time by MOBSE: we extract their masses and the delay time t_{delay} between progenitors' formation and their final merger. Finally we extract and store the total initial mass M_{BSE} of the stellar population

with the same metallicity simulated by MOBSE for each run.

Through a Monte Carlo code we associate a number $N_{CO,i}$ of compact objects binaries simulated with MOBSE to Illustris particles, following the algorithm

$$N_{CO,i} = N_{BSE,i} \frac{M_{Ill}}{M_{BSE}} f_{corr} f_{bin}$$

where i = BHB, DNS or NSBH, $N_{BSE,i}$ is the number of merging compact object simulated with MOBSE for each run, $f_{corr} = 0.285$ is a factor used to take into account that we simulate stars with $M_\star > 5$ $M_\odot$ and $f_{bin} = 0.5$ accounts for the fact that we simulate stars in binaries, which are assumed to be 50% of the total. We notice that by definition the quantity

$$n_{CO,i} = \frac{N_{BSE,i}}{M_{BSE}} f_{corr} f_{bin}$$

is the number of merging compact objects per unit stellar mass at a given metallicity. We find then the best match between Z_{Ill} and the set of 12 metallicities included in MOBSE (Mapelli et al. 2017 showed how this association will not affect the rate of merging compact objects). We provide an estimation of the lookback time at which the merger occurred as $t_{merg} = t_{form} - t_{delay}$, where t_{form} is the lookback time at which the Illustris' particle formed, given by:

$$t_{form} = \frac{1}{H_0} \int_0^{z_{Ill}} \frac{1}{(1+z)[\Omega_m (1+z)^3 + \Omega_\Lambda]^{1/2}} dz$$

with cosmological parameters consistent with Illustris' ones. Precisely, t_{merg} indicates how far away from us the merger between the compact objects occurred. In our study we take into account only for those compact objects which have merged within a Hubble time, i.e. $t_{merg} > 0$, and do not consider future mergers.

Chapter 3

Results

For the analysis of the environment surrounding compact-objects binaries, we focus on the mass of the host galaxies where the progenitor stars form M_{form}, the mass of the host galaxies where the compact objects merge M_{merg}, the metallicity of progenitors Z, the time when they form t_{form} and the time when they merge t_{merg}. In order to study the properties of host galaxies and progenitors, we have to find out in which galaxy our simulated binaries of compact objects merge. We use a Python script which obtain a list and store the above-mentioned properties of host galaxies and progenitors from the first downloaded snapshot of the Illustris simulation at $z \sim 16$ till a given snapshot, which corresponds to a certain redshift. We lead this analysis for 3 different merger redshifts $z \sim 0.01$, $z \sim 2$ and $z \sim 4$, which means that we study the distribution of compact objects merging at $z \sim 0.01$, $z \sim 2$ and $z \sim 4$. We remind the reader that $z \sim 2$ is the epoch at which the maximum peak of cosmic SFR occurred. In this way we are able to find any possible correlation and examine how they may change across cosmic time. We investigate BHBs, NSBHs and DNSs separately.

In this Chapter, we show our estimates of cosmic merger rate for BHBs, NSBHs and DNSs (Section 3.1) and the results of our analyses led for the cosmic times at $z \sim 0.01$ (Section 3.2), $z \sim 2$ (Section 3.3) and $z \sim 4$ (Section 3.4).

3.1 MZR Change and Merger Rate

The first goal we want to achieve is reproducing the cosmic merger rate in function of redshift for the three populations of compact-objects binaries: BHB, NSBH and DNS. As showed by Mapelli & Giacobbo (2018), only assuming low kick and values for $\alpha \geqslant 3$ our estimate for DNS merger rate agrees with the rate inferred from GW170817 by Abbott et al. (2017). A weak kick can preserve the binary from breaking, while a large value for α implies an efficient CE ejection with the prevention of a merger after CE phase. BHB and NSBH merger rate are instead in agreement with LIGO's predictions even for higher kicks and other reasonable values for α and λ. Having ascertained that, in our analysis we thus set the parameters for the CE formalism and core collapse to $\alpha = 5$, $\lambda = 0.1$ (thus $\alpha\lambda = 0.5$), $\sigma_{CCSN} = 15$ km s^{-1} using rapid-collapse prescription.

Furthermore, as mentioned above, the Illustris mass-metallicity relation is not in perfect agreement with the one found with observational data. We thus replace the MZR of the Illustris with the one adopted by Maiolino et. al (2008), calibrated on the AMAZE program results:

$$12 + \log(O/H) = -0.0864(\log M_\star - \log M_0)^2 + K_0$$

where M_0 and K_0 are parameters determined at each redshift by best-fits with observed

Table 3.1: Best-fit parameters for the mass-metallicity relation obtained by Maiolino et al. (2008) at different redshifts.

z	$\log M_0$	K_0
0.07	11.18	9.04
0.7	11.57	9.04
2.2	12.38	8.99
3.5[a]	12.76	8.79
3.5[b]	12.87	8.90

[a,b] Values obtained by using the masses estimated with two different templates.

data points (Table 3.1). In order to conform with observational results, we introduce also a spread in the particle metallicity, from a Gaussian function whose average metallicity equals the observational one and with standard deviation 0.3 dex.

In order to obtain the merger rate R_i (where i= BHB, NSBH or DNS), we extract the number of mergers N_i per time bin and then calculate it using the formula:

$$R_i = N_i \left(\frac{l_{box}}{Gpc}\right)^{-3} \left(\frac{\Delta t}{yr}\right)^{-1}$$

where $l_{box} = 106.5$ Gpc is the length of Illustris box and $\Delta t = 10$ Myr is the dimension of each time bin, from $z = 0$ till $z \sim 16$.

Simulations' outcomes are shown in Figure 3.1, 3.2 and 3.3 for BHBs, NSBHs and DNSs respectively. We clearly see how the merger rate for all investigated binaries increases with redshift till a maximum peak around $z \sim 2 - 4$, time at which it is believed the highest star formation rate occurred. BHBs and NSBHs have a steeper increase in merger rate going back in time compared to DNSs because of their stronger dependence on progenitor stars' metallicity.

Mapelli et al. (2017) estimated that the impact of the MZR exchange on the BHB merger rate should be on the order of 20%. Since DNS merger rate is almost indipendent on metallicity of the progenitors, it should not be significantly affected by the change.

In this Thesis, we first check the discrepancy between the merger rate obtained with the observational MZR and the one obtained with the Illustris MZR also for NSBHs and DNSs, which were not analyzed by Mapelli et al. (2017). We find that a $\sim 40\%$ difference holds in the case of DNSs and NSBHs and a $\sim 25\%$ difference in the case of BHBs. Furthermore, we want to check another possible bias factor. In particular, we want to see whether this $\sim 40\%$ difference is a genuine result of the different MZR or it is a selection effect. In fact, if we want to use the observational MZR by Maiolino et al. (2008), we need to know the total stellar mass M_* of the host galaxy of the stellar binary. However, the sub-halo finder cannot associate a host galaxy to all Illustris stellar particles, because some of them are not found to be part of a resolved galaxy. This selection effect is particularly strong for metal-poor stellar particles, because they tend to be associated to low-mass galaxies, and low-mass galaxies are unresolved ($\ll 1000$ particles) in the Illustris. Thus, several metal-poor stellar particles are missing in the calculation of the merger rate based on the Maiolino MZR. In contrast, each stellar particle has its own Illustris metallicity; consequently, when we use the Illustris' genuine metallicity, we account for all particles and we do not miss metal-poor particles. Thus, our guess is that the merger rate obtained with the Maiolino MZR could be lower than the merger rate obtained from the Illustris metallicity not because of the intrinsic

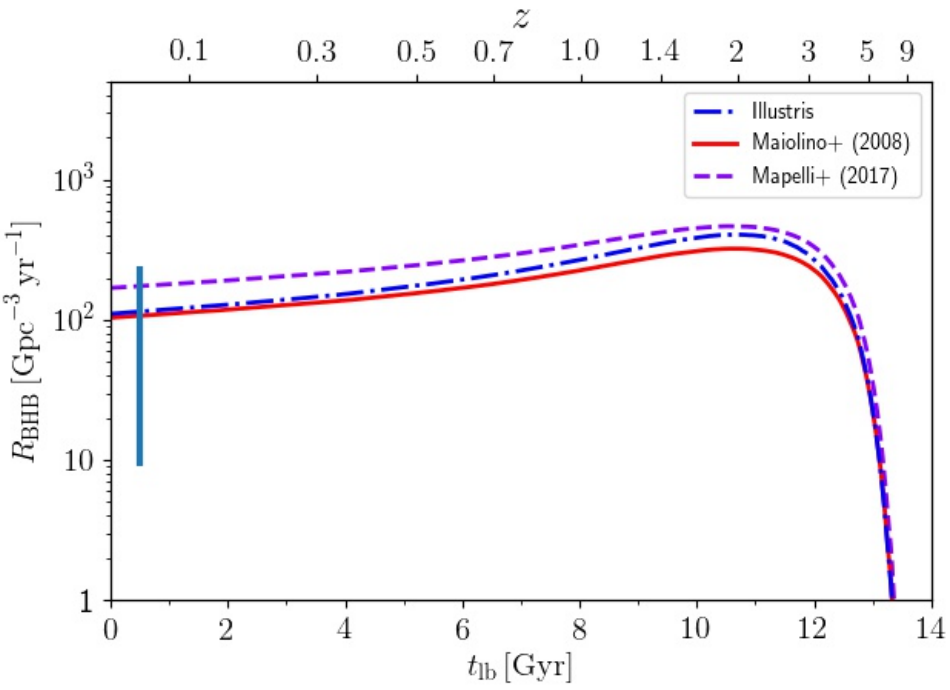

Figure 3.1: Merger rate obtained for BHBs in function of lookback time (bottom x axis) and redshift (top x axis) with the 2 MZRs adopted in our simulations and the results by Mapelli et al. (2017) for BHBs: *red* line for the observational MZR by Maiolino et al. (2008), dash-dotted *blue* line for the Illustris intrinsic MZR, dashed *violet* line for results by Mapelli et al. (2017). The error bar indicates LIGO's estimate of cosmic merger rate for BHBs from the O1 run.

difference between the two mass-metallicity relations, but because a large number of stellar particles (the ones which are not attributed to any host galaxy by the sub-halo finder) are not accounted for in our calculation based on the Maiolino MZR.

To check this we have calculated the merger rate using the genuine Illustris' metallicity but considering only the stellar particles which are associated to a galaxy by the sub-halo finder and we have compared it to the merger rate obtained with the Maiolino MZR. In this case, we compare two merger rates that were obtained considering exactly the same number of stellar particles. The results shown in Figures 3.1, 3.2 and 3.3 indicate that the difference between the two merger rates is now smaller than ~ 5 %, confirming our guess: the difference between the merger rates obtained with the Maiolino et al. (2008) MZR and the merger rates obtained with the Illustris metallicity are due to a selection effect (we cannot apply the observational MZR to particles which are not associated to a galaxy) more than to an intrinsic metallicity difference. This check strongly supports the robustness of our methodology.

3.2 $\mathbf{z \sim 0.01}$

The results described in this Section refer to compact objects that have formed anytime in the past and merged at $z \sim 0.01$; as a consequence, the merging lookback time for them is $t_{merg} \sim 0.1$ Gyr from now. Particular interest is given to correlations between $M_{form} - M_{merg}$,

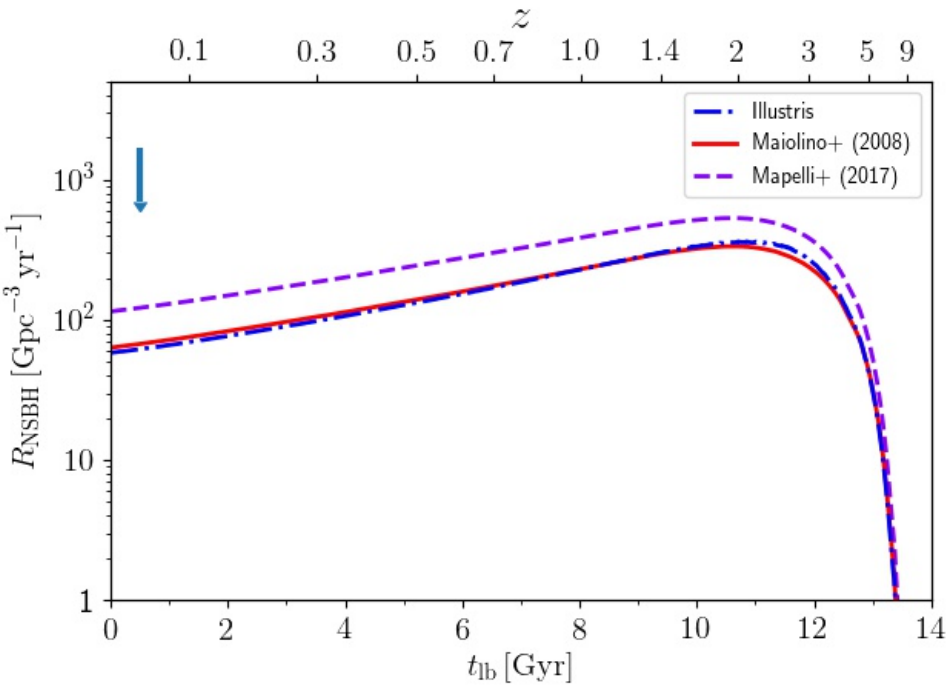

Figure 3.2: Merger rate obtained for NSBHs in function of lookback time (bottom x axis) and redshift (top x axis) with the 2 MZRs adopted in our simulations and the results by Mapelli et al. (2017) for NSBHs: *red* line for the observational MZR by Maiolino et al. (2008), dash-dotted *blue* line for the Illustris intrinsic MZR, dashed *violet* line for results by Mapelli et al. (2017). The error bar with the arrow indicates LIGO's upper-limit estimate of cosmic merger rate for NSBHs from the O1 run.

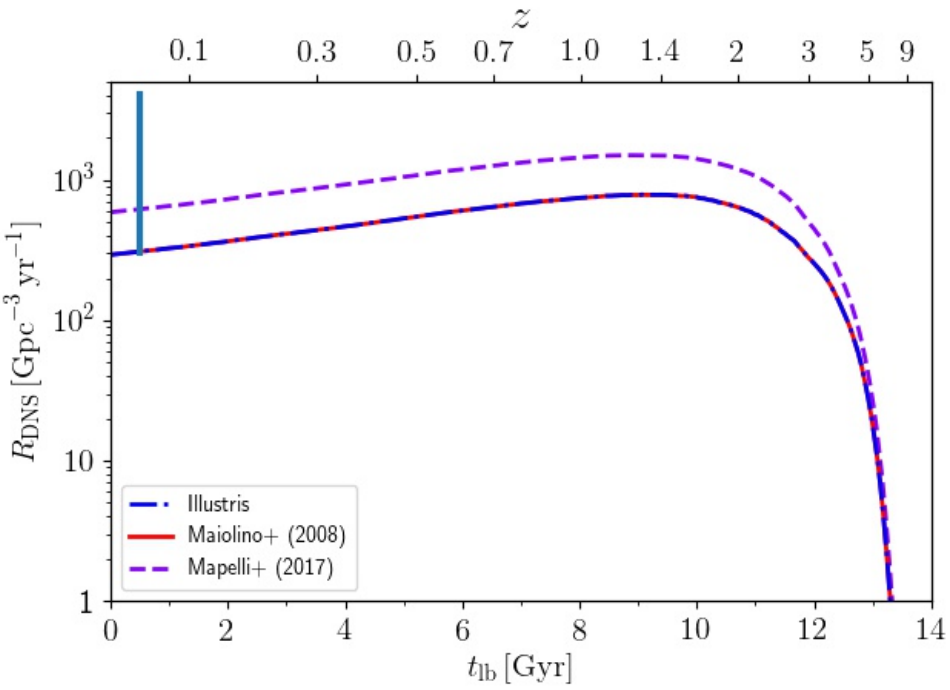

Figure 3.3: Merger rate obtained for DNSs in function of lookback time (bottom x axis) and redshift (top x axis) with the 2 MZRs adopted in our simulations and the results by Mapelli et al. (2017) for DNSs: *red* line for the observational MZR by Maiolino et al. (2008), dash-dotted *blue* line for the Illustris intrinsic MZR, dashed *violet* line for results by Mapelli et al. (2017). The error bar indicates LIGO's estimate of cosmic merger rate for DNSs from the O1 run.

$M_{form} - Z$, $M_{form} - t_{form}$, $M_{merg} - Z$ and $M_{merg} - t_{form}$. In this and in the following 2 Sections, every plot shows the above-mentioned properties on the axes and a color scale depicts the number of merger events at that redshift.

3.2.1 BHBs

Firstly, we want to check if there is any correlation between the mass of the host where the progenitors form and the mass of the host where BHBs merge (Figure 3.4). We distinctly see that the vast majority of the mergers occur in hosts which have mass higher (above-diagonal) or equal (on-diagonal) with respect to the hosts where the progenitor stars form. This is a clear hint for a formation channel of galaxies through Hierarchical Clustering (HC): bigger, thus massive structures form by subsequent mergers of smaller structures. This obviously implies that small structures form earlier in time while big ones form later.[1]

We notice from the plot that the majority of progenitors formed in galaxies with masses $10^7 - 10^9$ $M_\odot$ and the mergers mainly occurred in galaxies with masses from 10^8 $M_\odot$ to 10^{12} $M_\odot$. We point out that galaxies more massive than $\sim 10^{12}$ $M_\odot$ are yet to form. The apparent lack of mergers below 10^7 $M_\odot$ is likely due to Illustris low resolution at that regime; using a high-resolution simulation we will surely see a high number of mergers also for dwarf galaxies. The mergers under the diagonal, which represent those compact objects which have merged in galaxies with mass lower than that of formation, can be explained simply as a statistical fluctuation.

We are interested also to check the correlation between metallicity of progenitors and mass of host galaxies. From Figure 3.5 we clearly see the MZR: low-Z stars formed in low-mass galaxies and high-Z stars formed in high-mass ones. In particular we have a concentration of stars with $Z \sim 0.02 - 0.2$ $Z_\odot$ in galaxies with mass $\sim 10^8 - 10^9$ $M_\odot$. There is a clear cut at the metallicity highest value around $Z \sim 0.3$ $Z_\odot$.

In Figure 3.6 we plot instead M_{merg} against progenitors' metallicity Z. We see that the particles present in the plot $M_{form} - Z$ have been spread towards higher masses by the HC process. We still see a concentration of mergers (at $\sim 10^{11}$ $M_\odot$, $Z \sim 0.05 - 0.1$ $Z_\odot$) but if we considered future mergers, we would not see this concentration anymore and they would be homogeneously distributed on the $M_{merg} - Z$ plot.

Finally, we plot in Figure 3.7 the masses of the host galaxies where progenitors formed as a function of the formation time. We see that the majority of progenitors of BHBs that merge at $z \sim 0.01$ originates at lookback times around $t_{form} \sim 8 - 13$ Gyr. This means that on average the delay time from the formation epoch to the merger is of the order of $t_{delay} \sim 10$ Gyr for BHBs. From this we can deduce that there is a rather high likelihood that BHBs detected to merge nowadays by LIGO have formed a few billion years ago and needed a long time before the merger occurred.

3.2.2 NSBHs

We proceed with the same analysis for NSBHs which merged at $z \sim 0.01$. From the graph $M_{form} - M_{merg}$ (Figure 3.8) we see a correlation similar to the one for BHBs. NSBHs seem a bit more concentrated on the diagonal, which means that M_{form} coincides with the M_{merg}; so compared to BHBs' case, it is a little more likely that NSBHs form and subsequently merge either in the same host or in another host with the same mass. This is partially visible in

[1] Despite that, from observations we have proof of existence of massive early-type galaxies since the early epochs, around $z \sim 4$. As Neistein, van den Bosch & Dekel (2006) pointed out, this phenomenon is not necessarily in paradox with HC model. They showed it is a natural effect of the bottom-up process of dark-matter halos.

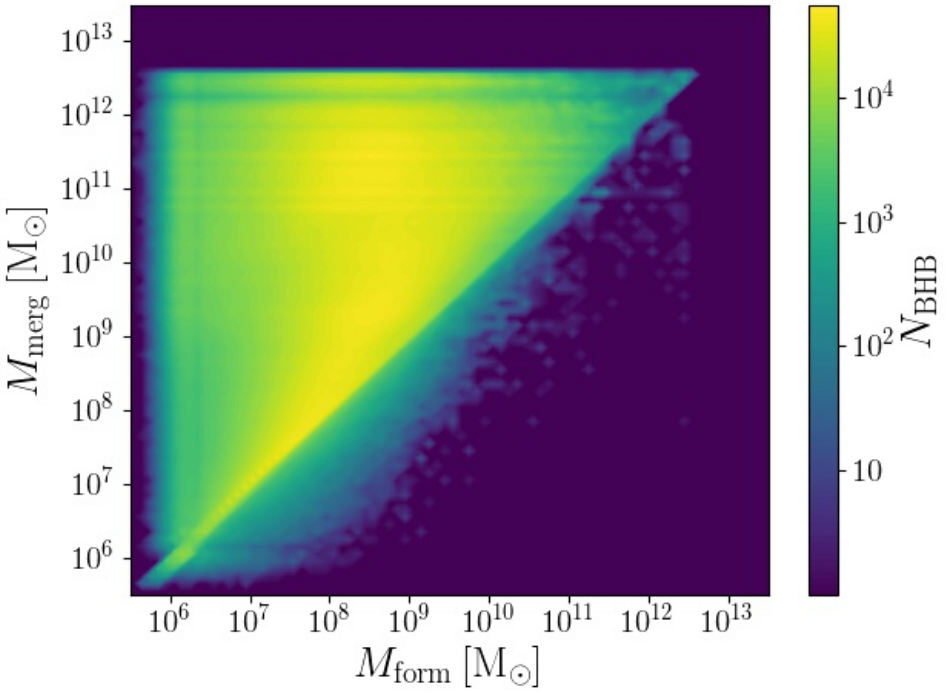

Figure 3.4: Plot showing the mass of the host where progenitor stars formed against the mass of the host where the BHBs merged.

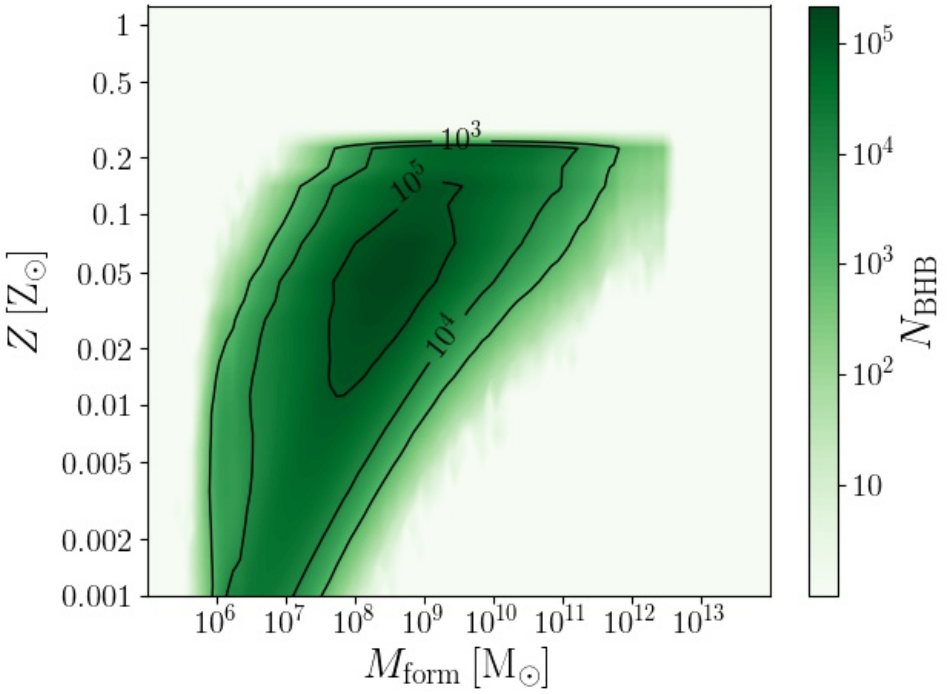

Figure 3.5: Plot showing the mass of the host where the progenitor stars of BHBs formed against their metallicity.

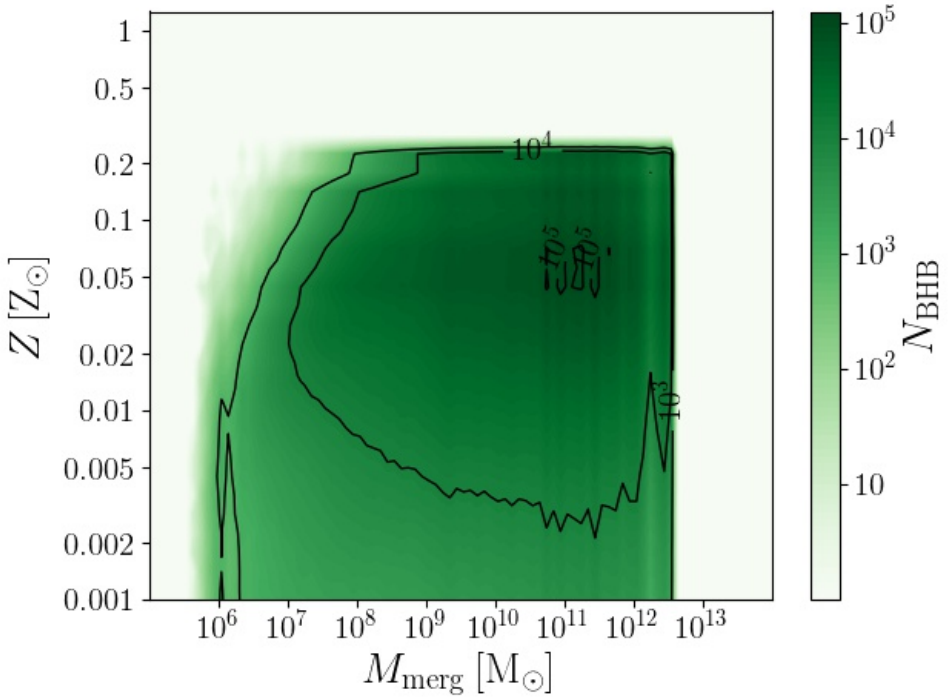

Figure 3.6: Plot showing the mass of the host where BHBs merged against progenitors' metallicity.

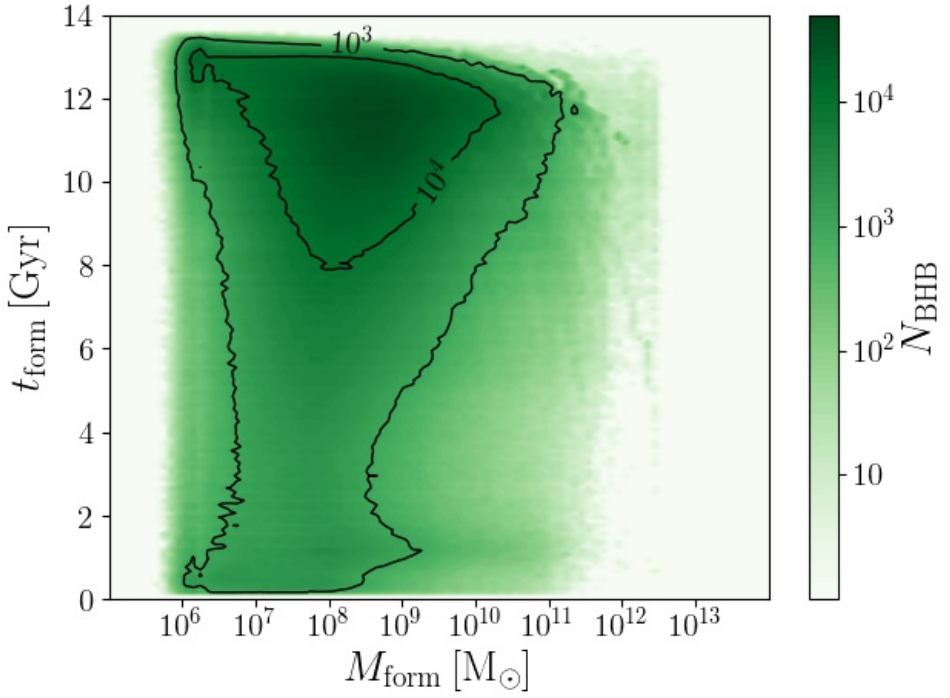

Figure 3.7: Mass of the formation host in function of the formation time of the progenitor stars of BHBs.

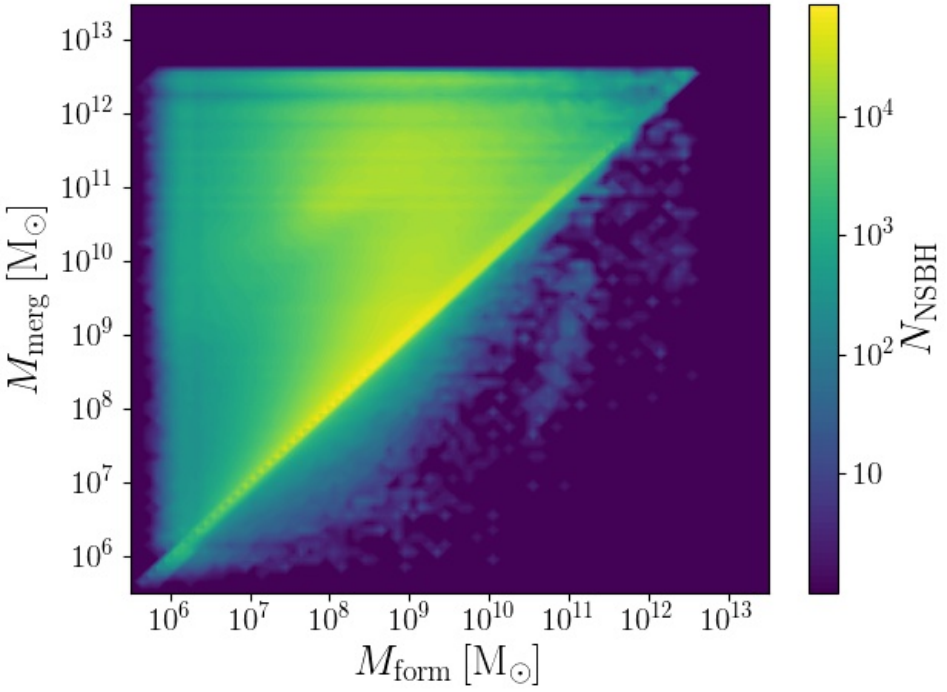

Figure 3.8: Plot showing the mass of the host where progenitor stars formed against the mass of the host where the NSBHs merged.

Figure 3.9: the concentration of NSBHs formed at $t_{form} \sim 10 - 12$ Gyr is weaker while there are a few more progenitors which formed around $t_{form} \sim 1$ Gyr, which results into a short delay time.

In Figure 3.10 we analyze the MZR for NSBHs. The slope and the spread of the MZR resemble the one found for BHBs but progenitors reach slightly higher metallicities, around $Z \sim 0.5$ Z$_\odot$; moreover, while in the graph $M_{mform} - Z$ BHBs seem to follow an approximately-linear distribution, NSBHs' MZR is peaked around $M_{form} \sim 10^9$ M$_\odot$ and $Z \sim 0.1 - 0.2$ Z$_\odot$.

Analogous is the behaviour in the plot $M_{merg} - t_{form}$ (Figure 3.11). Following the hierarchical channel for the formation of massive galaxies, we see how NSBHs' progenitors of any metallicity are distributed on galaxies of any mass, even if a preference for high Z/high M_{merg} still holds.

3.2.3 DNSs

Results for DNSs are quite different from the other 2 classes of compact objects. Starting with the $M_{form} - M_{merg}$ plot (Figure 3.12), we immediately see that the vast majority of mergers occurs in galaxies with the same mass as the formation one, specially in the range $M_{form} = M_{merg} \sim 10^9 - 10^{11}$ M$_\odot$. This may be a hint that DNSs merge into the formation host before it undergoes the effect of hierarchical clustering, meaning that the delay time for DNSs is shorter than the timescale for which mergers between galaxies take place. Analyzing the $M_{form} - t_{form}$ graph (Figure 3.13) we notice that, although DNSs' progenitors formed in the early universe as well as in recent epochs, there is clear predominance for formation at $t_{form} \lesssim 2$ Gyr, which implies a very short average delay time, in agreement with the outcome found above.

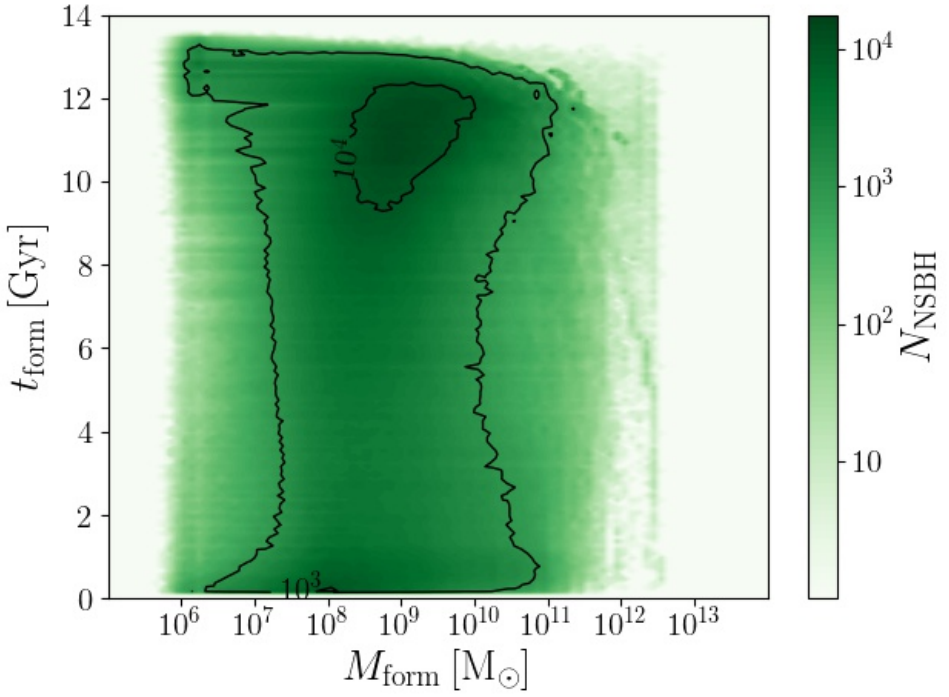

Figure 3.9: Mass of the formation host in function of the formation time of the progenitor stars of NSBHs.

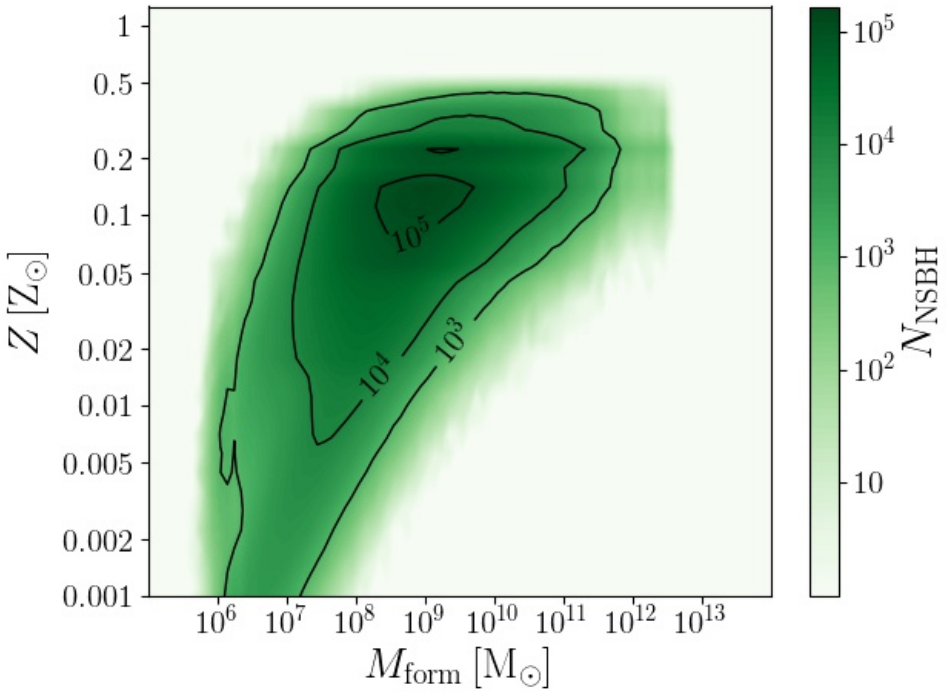

Figure 3.10: Plot showing the mass of the host where the progenitor stars of NSBHs formed against their metallicity.

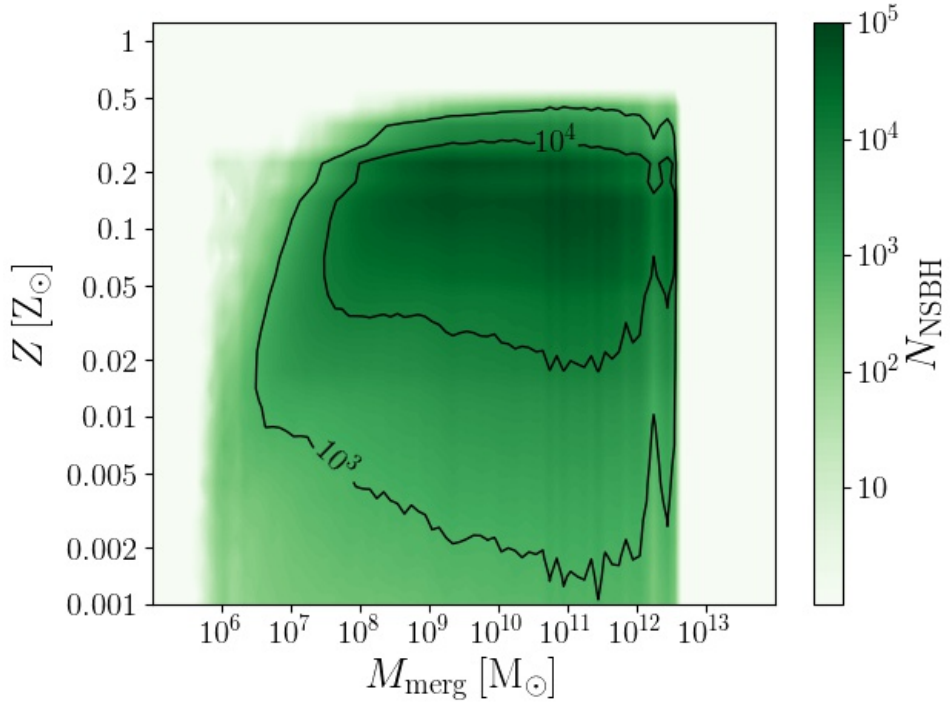

Figure 3.11: Plot showing the mass of the host where NSBHs merged against progenitors' metallicity.

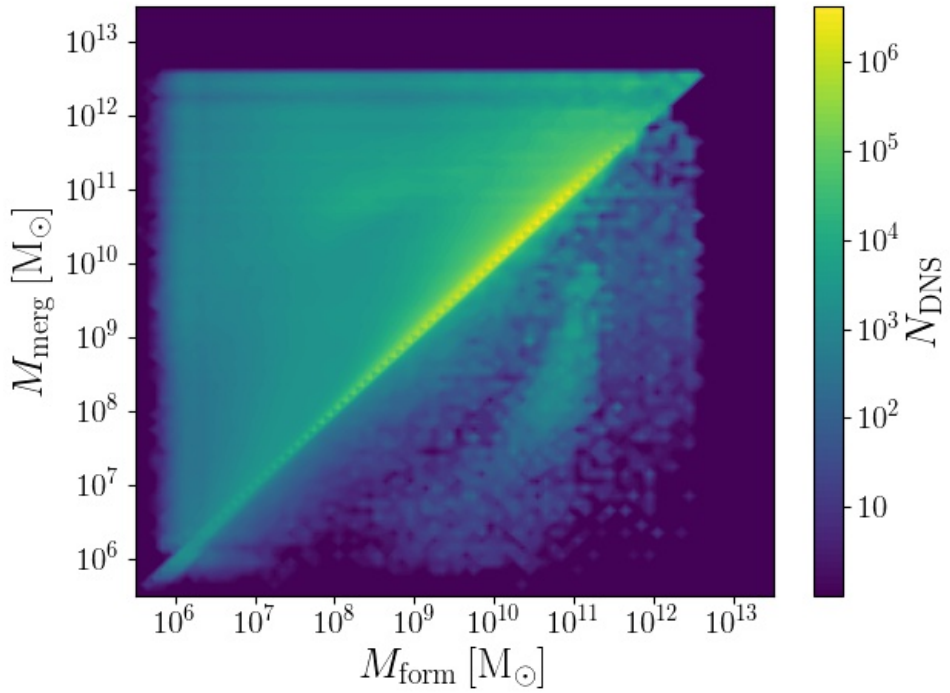

Figure 3.12: Plot showing the mass of the host where progenitor stars formed against the mass of the host where the DNSs merged.

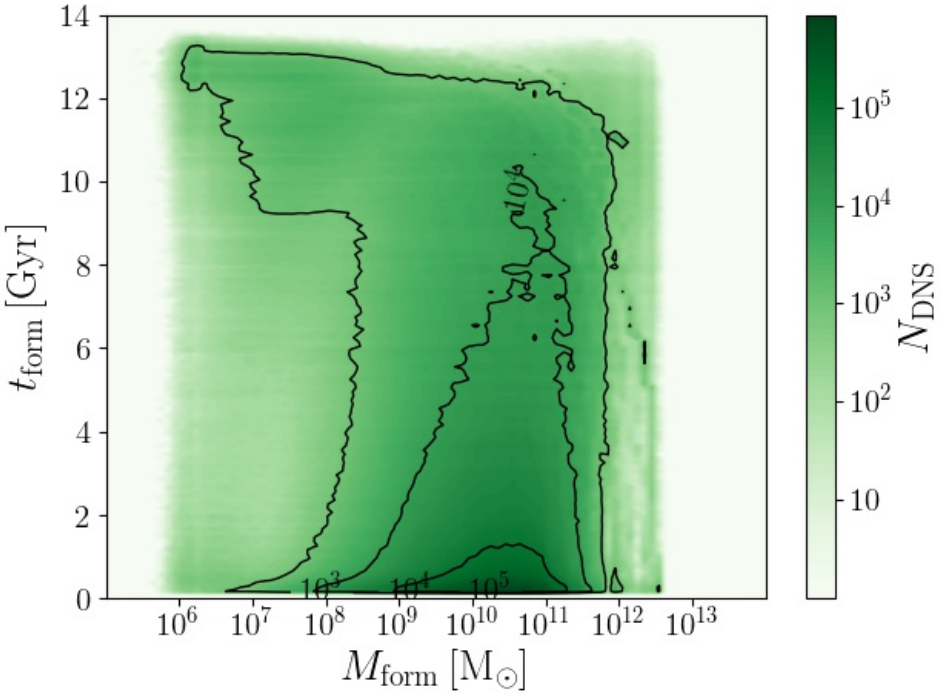

Figure 3.13: Mass of the formation host in function of the formation time of the progenitor stars of DNSs.

The Figure 3.14 shows the MZR followed by DNSs. We find low-metallicity progenitors in low-mass galaxies and vice versa. Progenitors' metallicity reaches very high values, till 20 times the solar one; in details, the majority of them formed in massive galaxies with $10^9 - 10^{11}$ $M_\odot$ and have metallicities in the range $Z \sim 0.5 - 5$ $Z_\odot$. There is no evidence of low-Z progenitors in massive galaxies at the epoch of their formation.

Looking at the plot $M_{merg} - Z$ (Figure 3.15) we see that DNSs whose progenitors had low metallicity can be found also in massive galaxies at the epoch of merger; these are only a small fraction of the total. The vast majority of progenitors had high-Z and did not move to more massive galaxies during the time elapsed between their formation and their merger; specifically, these progenitors are the ones with $Z \gtrsim 0.1$.

Combining the results for this plot with those extracted from the $M_{form} - M_{merg}$ and $M_{form} - t_{form}$ graphs, we obtain that the few DNSs which had low-metallicity progenitors are the ones which needed a long time before merging, and thus they belonged to a low-mass galaxy during their formation and either a low-mass or massive galaxy at the epoch of merger. On the other hand, high-Z progenitor stars formed later in already-massive galaxies and merged after a short time.

We want to remind that the event GW170817, detected in first place through gravitational waves, has been associated to an electromagnetic signal spanning from gamma rays to radio wavelengths. This led to the identification of the host galaxy, NGC 4993. The mass range in which we foresee to find merging DNSs is consistent with the typical mass of galaxies from which we detect emission of short gamma-ray bursts ($10^{8.5} - 10^{12}$ $M_\odot$, Leibler & Berger 2010; Berger 2014; Troja et al. 2016); in particular, NGC 4993 has an estimated stellar mass of $0.3 - 1.2 \times 10^{11}$ $M_\odot$. These results are described in Mapelli, Giacobbo, Toffano et al. (2018).

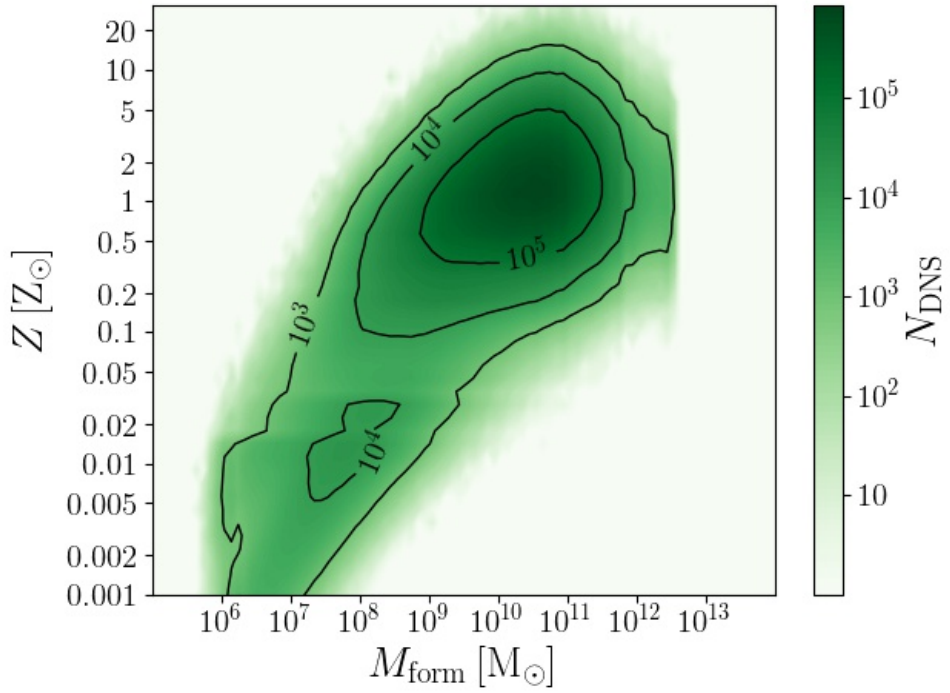

Figure 3.14: Plot showing the mass of the host where the progenitor stars of DNSs formed against their metallicity.

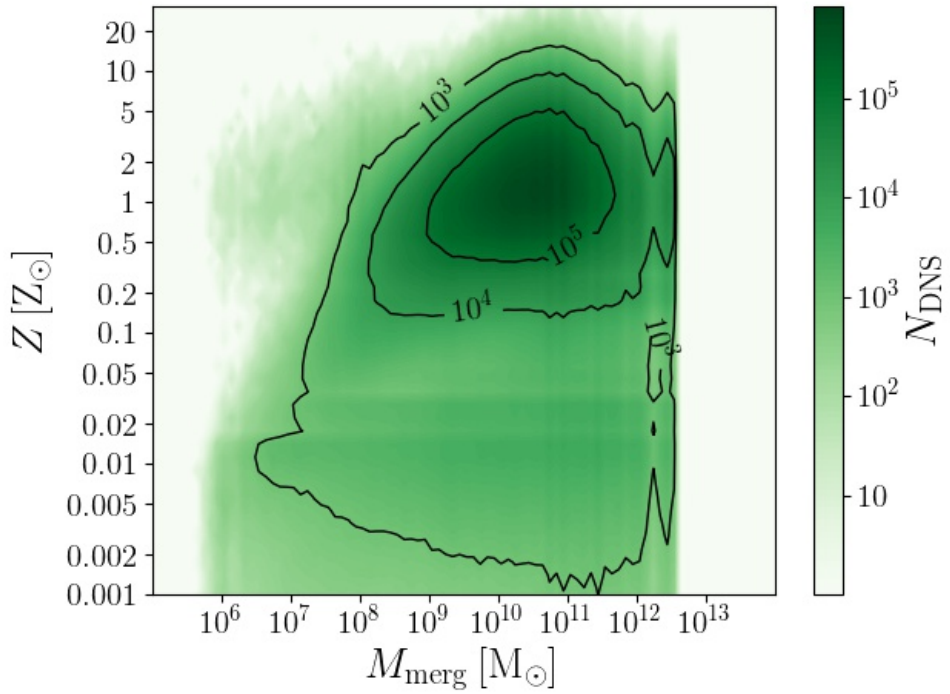

Figure 3.15: Plot showing the mass of the host where DNSs merged against progenitors' metallicity.

3.3 z ∼ 2

In this Section we analyze compact objects that merged at $z \sim 2$, which corresponds to a lookback time $t_{merg} \sim 10.4$ Gyr. As in the previous Section, we focus on correlation between $M_{form} - M_{merg}$, $M_{form} - Z$, $M_{form} - t_{form}$, $M_{merg} - Z$ and $M_{merg} - t_{form}$. In few plots we observe small structures like the mass gap we see at $M_{merg} \sim 10^{12}$ $M_\odot$ in the plots $M_{merg} - Z$ and $M_{form} - M_{merg}$; we can easily explain them as statistical fluctuations due to the low amount of simulated mergers having used a minor number of Illustris snapshots. These flaws are visible for BHBs, NSBHs and DNSs but are not worth taking care of.

3.3.1 BHBs

We start with the plot $M_{form} - M_{merg}$ (Figure 3.16). We notice the same pattern seen for BHBs merged at $z \sim 0.01$ with few differences. As predicted by our outcome for the cosmic merger rate, we see a total higher number of mergers in this epoch; moreover, although we see many BHBs above the diagonal, mainly formed in galaxies with masses $10^7 - 10^9$ $M_\odot$ and merged in more massive galaxies, a large fraction of them are on the diagonal or close to it. This means that they merged in the same galaxy where they formed or in a slightly more massive one, which may be the formation galaxy that accreted by means of HC process, in both cases implying short delay times. This can be quite obvious since we are studying BHBs merged around 10 Gyr ago, with an estimated life of the universe by reliable cosmological models around 13.6 Gyr.

As visible in the $M_{form} - t_{form}$ plot in Figure 3.17, the distribution of the formation time of the progenitors of BHBs merged at $z \sim 2$ is quite homogeneous as a first approximation. The merging BHBs formed between $\sim$ 13.6 Gyr ago and $\sim$ 10.5 Gyr ago in galaxies with masses of $10^6 - 10^{11}$ $M_\odot$, with a concentration at $10^7 - 10^9$ $M_\odot$. This is also the range in the plot $M_{form} - M_{merg}$ where we have the highest number of mergers on the diagonal. Thus we conclude that those BHBs merged at $z \sim 2$ in galaxy with masses $10^7 - 10^9$ $M_\odot$ formed mainly $\lesssim$ 13 Gyr ago, consequently with a delay time of $t_{delay} \lesssim 2.5$ Gyr.

In Figure 3.18 and 3.19 we plot the metallicity of progenitors against the mass of the host galaxy where they formed and where they merged respectively. In the first plot we do not notice relevant difference from the results obtained for BHBs merged at $z \sim 0.01$, if not the higher number of mergers and the lower mass of the host galaxies, as explained above. Progenitors' metallicity is in the same range $Z \sim 0.001 - 0.3$.

We notice in the second plot that a sort of correlation is still present between M_{merg} and Z. We have seen in the previous Section how the HC process does spread the particles in the $M_{form} - Z$ plot towards higher masses, making their distribution more homogeneous. At $z \sim 2$ the process has not had time enough to homogenize it, so we still see a sort of MZR, this time between M_{merg} and Z. We still have an abundance of low-Z progenitors which merged in low-mass galaxies and vice versa, even if the number of low-Z progenitors merged in massive galaxies is no more negligible. Finally, we notice that at $z \sim 2$ the most massive galaxies have a mass of the order of 10^{12} $M_\odot$.

3.3.2 NSBHs

The results found for NSBHs merging at $z \sim 2$ are very close to the ones found for BHBs. From Figure 3.20 we see that Illustris particles are distributed on the diagonal or above it. As found for the $z \sim 0.01$ case, there are a few more mergers which occurred in galaxies with same mass as the formation one compared to BHBs. Moreover, the bulk of the distribution is slightly shifted towards higher masses, around $10^8 - 10^{10}$ $M_\odot$. In Figure 3.21 we notice how

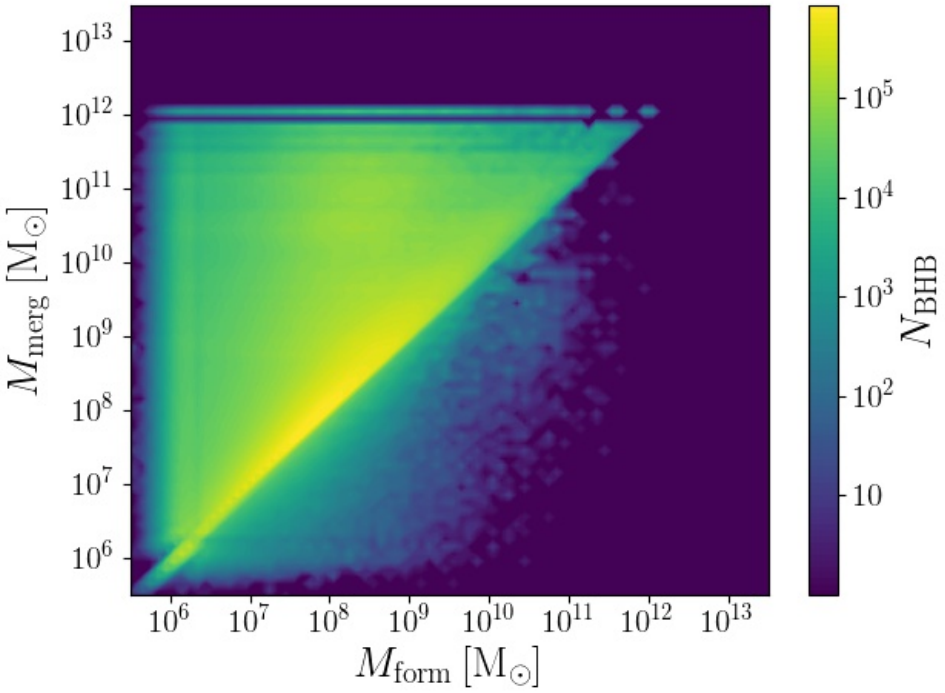

Figure 3.16: Plot showing the mass of the host where progenitor stars formed against the mass of the host where the BHBs merged at $z \sim 2$.

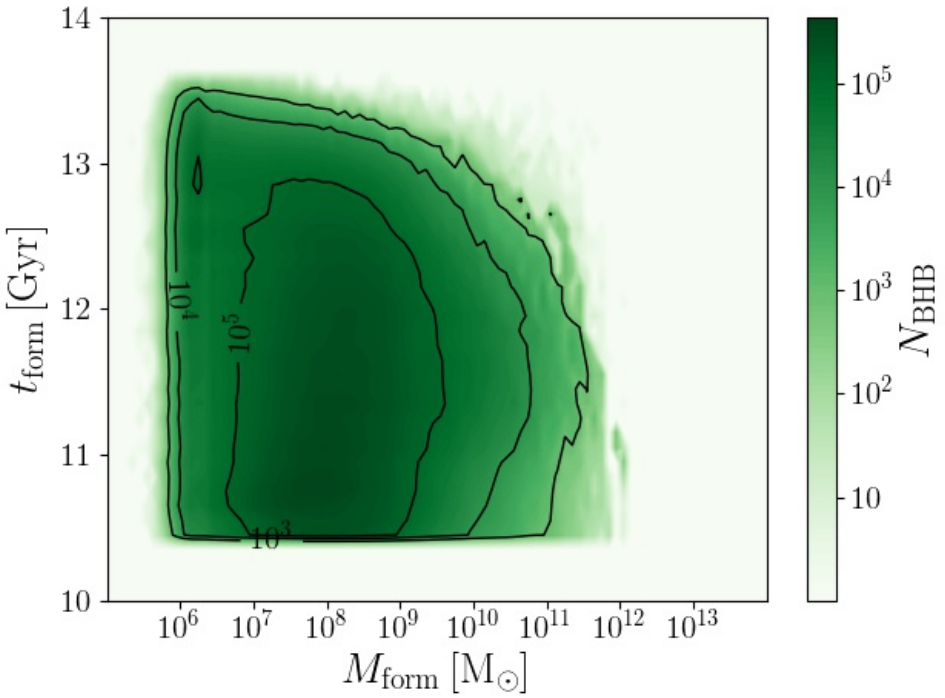

Figure 3.17: Mass of the formation host in function of the formation time of the progenitor stars of BHBs which merged at $z \sim 2$.

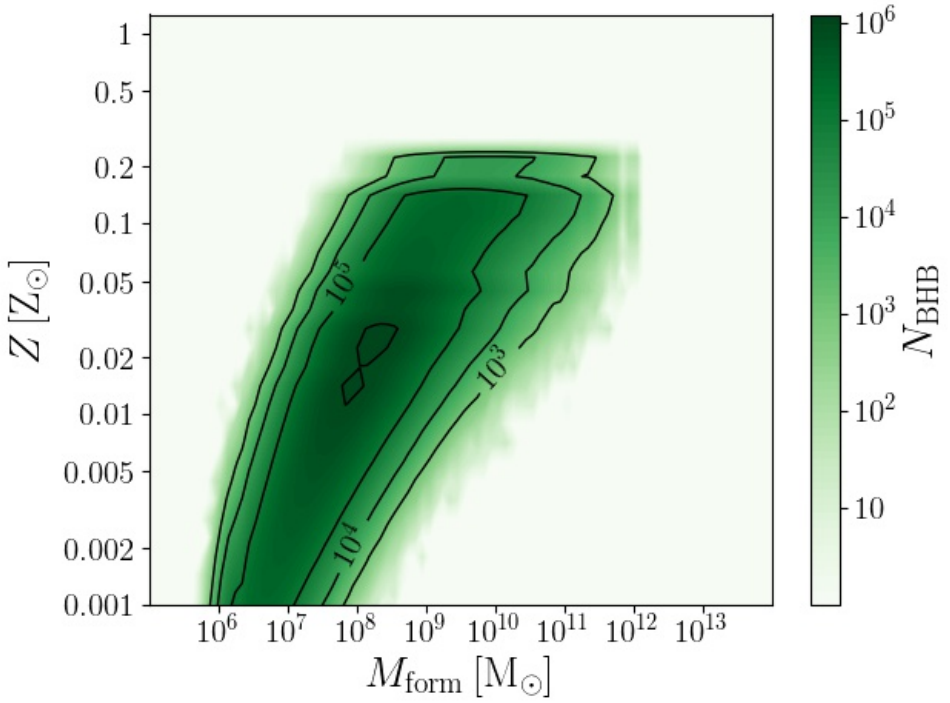

Figure 3.18: Plot showing the mass of the host where the progenitor stars of BHBs merged at $z \sim 2$ formed against their metallicity.

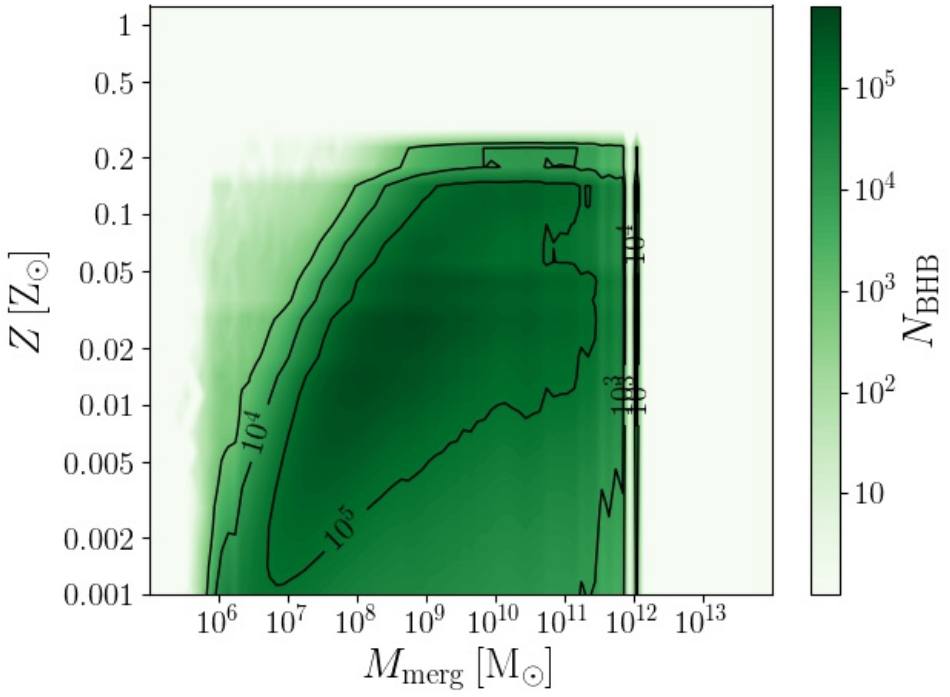

Figure 3.19: Plot showing the mass of the host where BHBs merged at $z \sim 2$ against progenitors' metallicity.

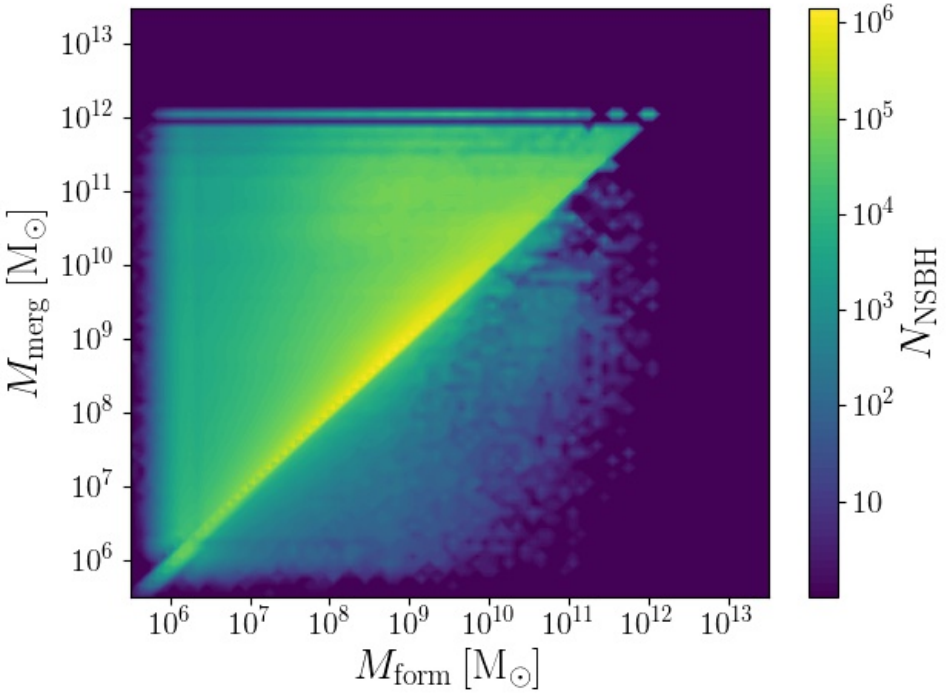

Figure 3.20: Plot showing the mass of the host where progenitor stars formed against the mass of the host where the NSBHs merged at $z \sim 2$.

these on-diagonal mergers may be the ones with shorter delay time $t_{delay} \sim 2$ Gyr. Apart from this peak in the distribution, it seems that NSBHs progenitors formed quite homogeneously across the whole mass range at any epoch before the merger; we want to remark that they could not form in galaxies with mass around $\gtrsim 10^{12}$ M$_\odot$ in the early ages since such massive ones do not exist yet.

We show in Figure 3.22 the MZR for NSBHs merged at $z \sim 2$. We see the usual direct proportionality between Z and M_{form} and the predominance for NSBHs to be distributed on the central region of the distribution, between $M_{form} \sim 10^7 - 10^{11}$ M$_\odot$ and $Z \sim 0.002 - 0.2$ Z$_\odot$. Compared to NSBHs which merged at $z \sim 0.01$, we notice that the peak in the distribution is much less marked here.

For the $M_{merg} - Z$ plot (Figure 3.23) we obtain almost the same results as for BHBs which merged at $z \sim 2$. We see that NSBHs with low-Z progenitors merged also in massive galaxies, but the majority of merger occurred in the mass range $10^8 - 10^{11}$ M$_\odot$ and metallicity range $0.01 - 0.2$ Z$_\odot$. So the majority of progenitors which formed in galaxies in these ranges of mass and metallicity are likely the ones that merged after a shorter delay time ($\lesssim 2$ Gyr) with respect to the others (~ 3 Gyr).

3.3.3 DNSs

We study now the environment for DNSs merged at $z \sim 2$. We plot the graph $M_{form} - M_{merg}$ in Figure 3.24. We clearly notice that, as well as in the $z \sim 0.01$ case, the vast majority of mergers occurred in galaxies with the same masses as the formation galaxies through the whole mass range but specially between $\sim 10^9$ M$_\odot$ and $\sim 10^{12}$ M$_\odot$. The fraction of mergers occurred away from the diagonal is $\lesssim 1\%$ of the total.

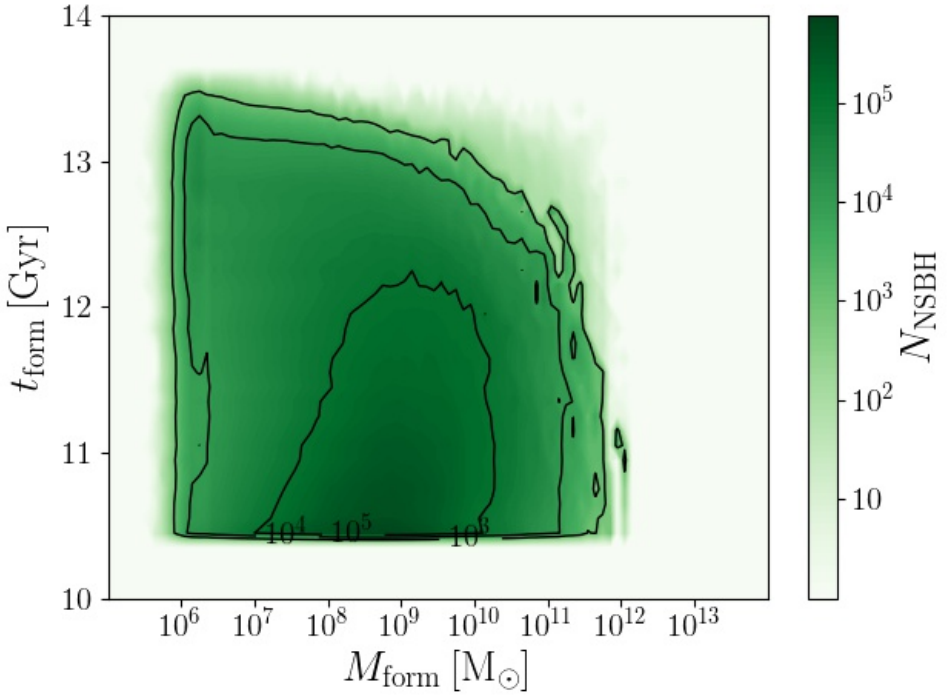

Figure 3.21: Mass of the formation host in function of the formation time of the progenitor stars of NSBHs which merged at $z \sim 2$.

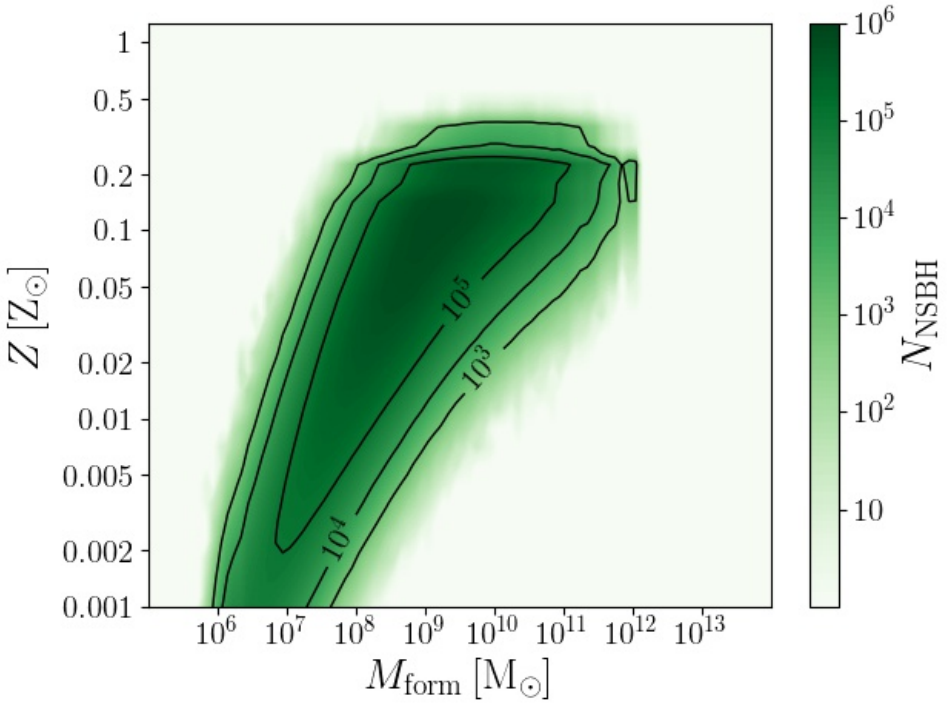

Figure 3.22: Plot showing the mass of the host where the progenitor stars of NSBHs merged at $z \sim 2$ formed against their metallicity.

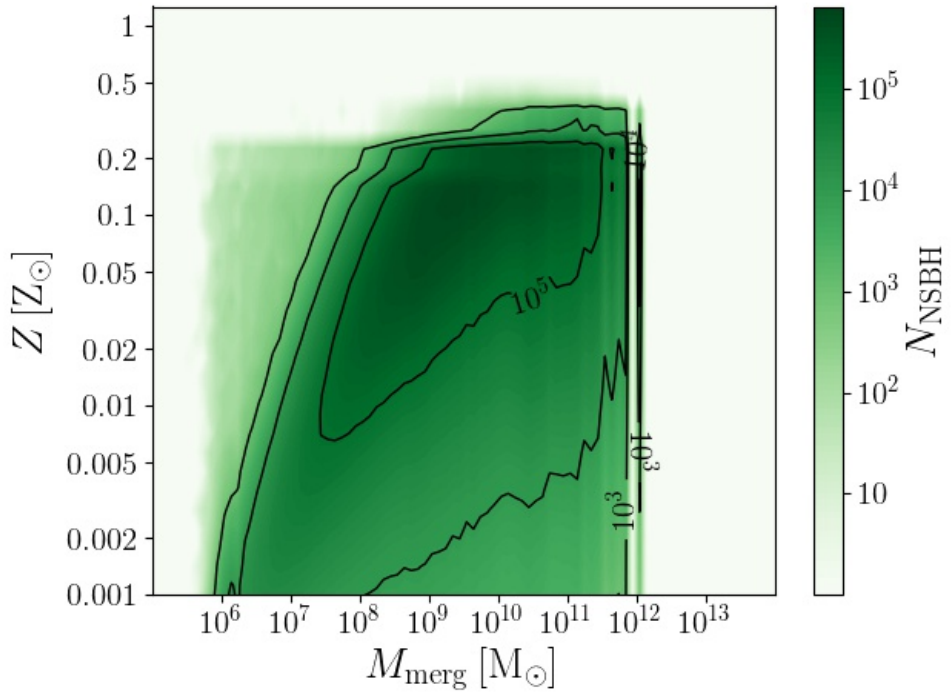

Figure 3.23: Plot showing the mass of the host where NSBHs merged at $z \sim 2$ against progenitors' metallicity.

As done above, we search for possible correlations in the plot $M_{form} - t_{form}$ (Figure 3.25). We see that mergers occurred in those mass ranges are the ones with shortest delay time: progenitors formed less than 12 Gyr ago and merged around 10.5 Gyr ago, resulting into a delay time $t_{delay} \lesssim 1.5$ Gyr. The remaining fraction of progenitors which merged at $z \sim 2$ is uniformly distributed in the range $t_{form} \sim 10.5 - 13.6$ Gyr.

In Figure 3.26 we analyze the MZR. Metallicities reached by progenitor stars are as high as the ones found for mergers occurred at $z \sim 0.01$, around 20 $Z_\odot$, and the shape of the MZR is analogous. A clear difference consists in the distribution of the particles: while in the $z \sim 0.01$ case we had a significant peak at $Z \sim 0.5 - 5$ $Z_\odot$ and $M_{form} \sim 10^9 - 10^{11}$ $M_\odot$, here we see that there is a substantial fraction of particles with low metallicity. Going back in time to high redshifts we find more low-metallicity stars than at present day; since it is most likely that DNSs form and merge after a short delay time, their progenitors will have a low Z in ancient epochs while predominantly high Z in recent ones.

Analyzing the plot $M_{merg} - Z$ in Figure 3.27 we notice a pattern similar to the one found for DNSs which merged at $z \sim 0.01$: for high-Z progenitors the merger occurred in the same galaxy where they formed, while for low-Z ones it took place either in a low-mass or massive host. So, as obtained for DNSs which merged at $z \sim 0.01$, we derive that progenitors with high-Z are the ones who formed and merged in massive galaxies in a short time, while low-Z progenitors needed a longer time to reach the merger phase and thus they formed in low-mass galaxies and merged either in low-mass or massive ones. The crucial difference is that low-Z stars were more common at those epochs than nowadays, so the fraction of low-Z progenitors is no more negligible; moreover, the distinction between high- and low-metallicity progenitors here occurs at $Z \sim 0.02$ $Z_\odot$, against the value $Z \sim 0.05 - 0.1$ $Z_\odot$ for the case $z \sim 0.01$.

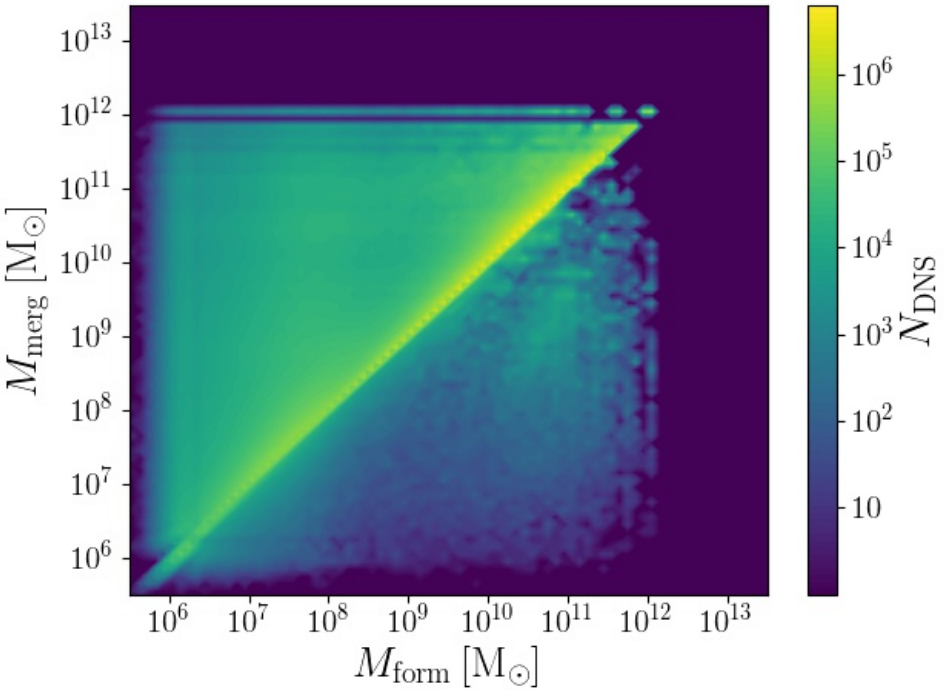

Figure 3.24: Plot showing the mass of the host where progenitor stars formed against the mass of the host where the DNSs merged at $z \sim 2$.

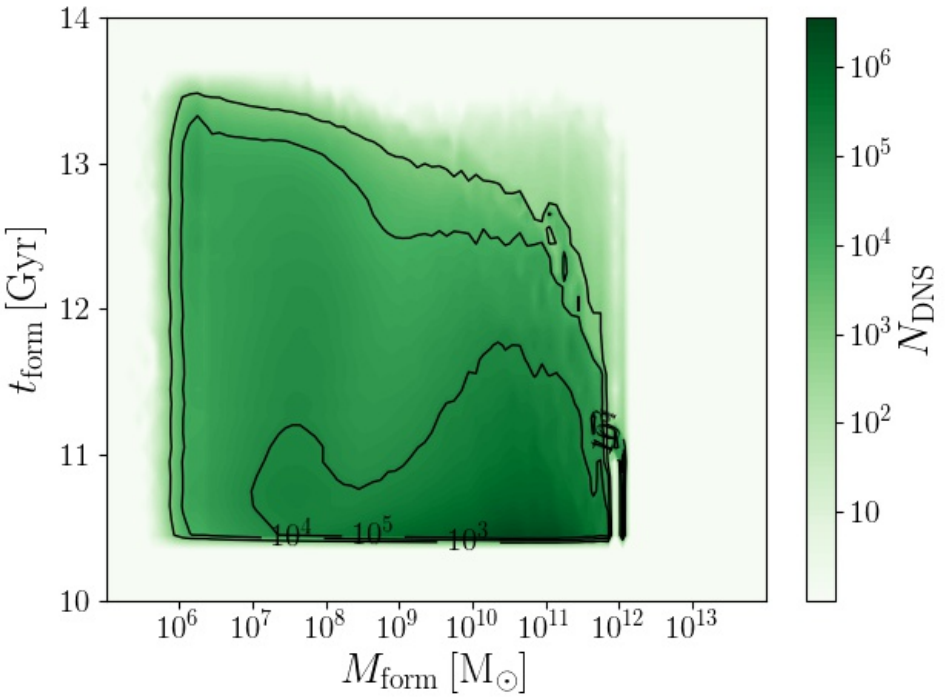

Figure 3.25: Mass of the formation host in function of the formation time of the progenitor stars of DNSs merged at $z \sim 2$.

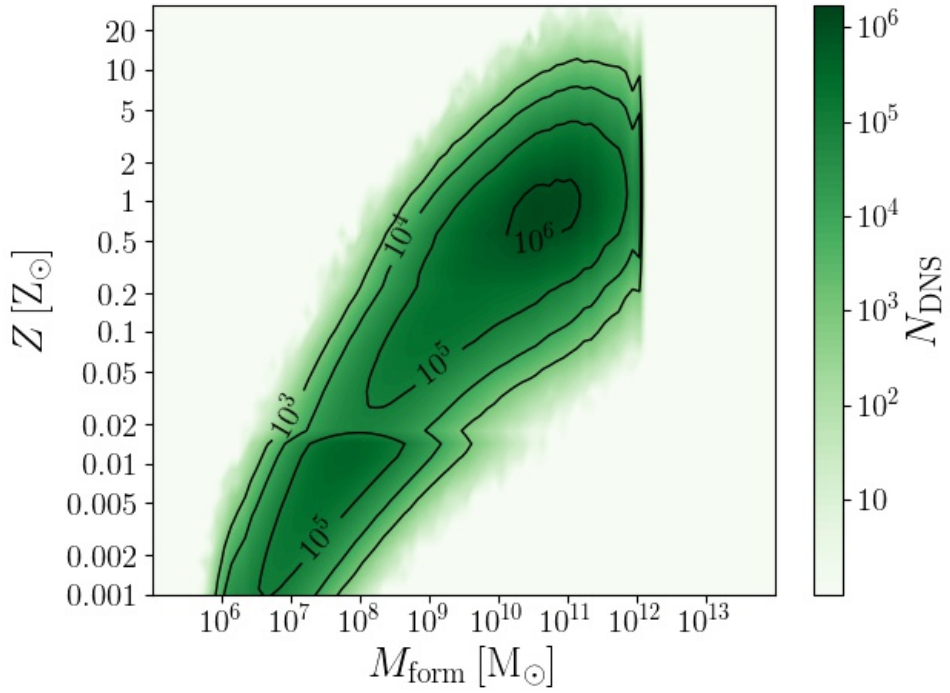

Figure 3.26: Plot showing the mass of the host where the progenitor stars of DNSs merged at $z \sim 2$ formed against their metallicity.

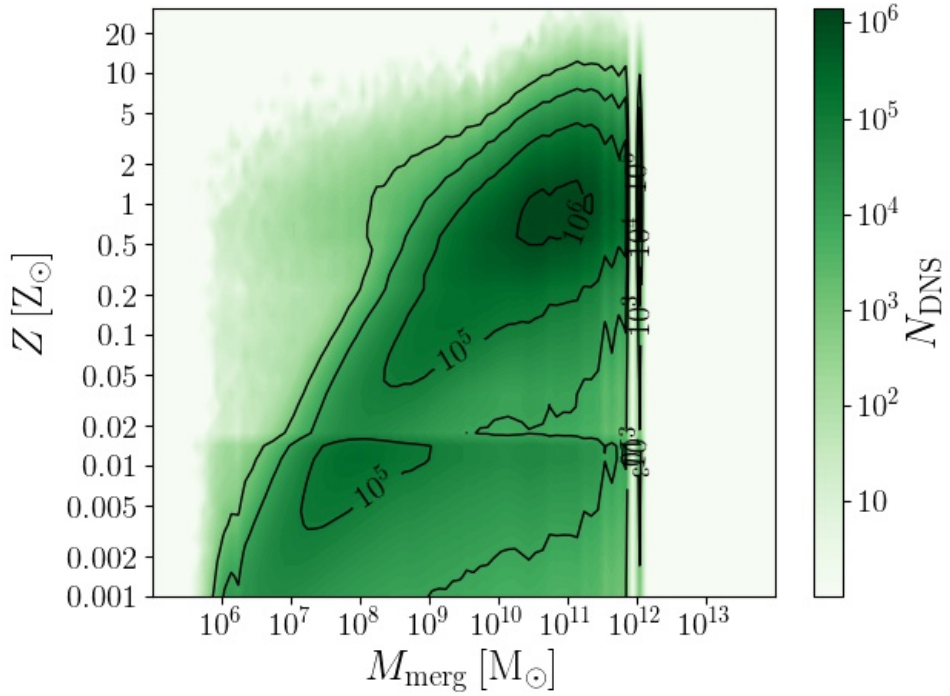

Figure 3.27: Plot showing the mass of the host where DNSs merged at $z \sim 2$ against progenitors' metallicity.

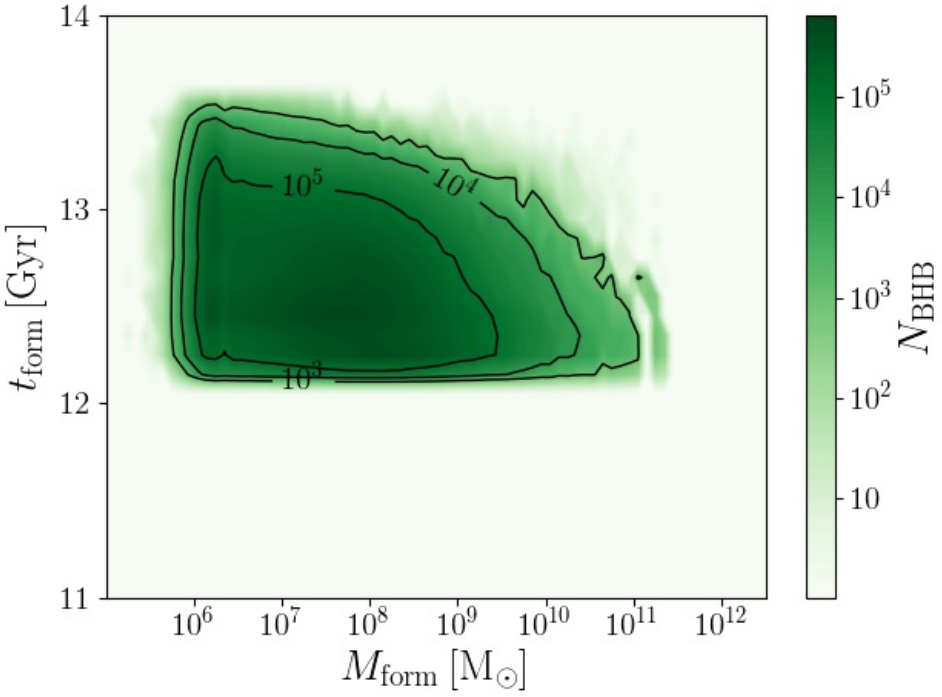

Figure 3.28: Mass of the formation host in function of the formation time of the progenitor stars of BHBs which merged at $z \sim 4$.

3.4 z ∼ 4

In this Section we study the environment of compact objects which merged at $z \sim 4$, that corresponds to a lookback time $t_{merg} \sim 12.2$ Gyr. We perform the same analysis as did for $z \sim 0.01$ and $z \sim 2$. Given the low number of Illustris particles present in the snapshots, statistical defects are a bit augmented in the following plots; as above, they have to be ignored.

3.4.1 BHBs

Firstly we focus on $M_{form} - t_{form}$ plot (Figure 3.28). Since mergers occurred at $z \sim 4$, delay times must be $\lesssim 1.4$ Gyr; in particular, most of the progenitors formed in low- or intermediate-mass galaxies $M_{form} \sim 10^6 - 10^9$ $M_\odot$ and show a preference for $t_{delay} \lesssim 1.0$ Gyr. Since the most massive galaxies assemble later in time, we naturally have that the fraction of progenitors which formed in massive ones is a minority.

From the $M_{form} - M_{merg}$ plot in Figure 3.29, we see again that the vast majority of mergers occurred in galaxies with masses equal or higher than the formation host. Since the short delay time, we do not properly see the build-up effect of HC, thus mergers are mainly distributed on the diagonal or close to it in the plot.

We look now at the MZR in Figure 3.30. While the slope seems to be about the same as the $z \sim 0.01$ case, we notice that the spread on the x-axis is lower and the distribution is less concentrated. The metallicity range still spans from ~ 0.001 $Z_\odot$ to ~ 0.3 $Z_\odot$. This pattern is also visible in the $M_{merg} - Z$ plot (Figure 3.31). Due to the short delay time, only a fraction of particles moved towards higher masses and thus we still see a correlation between the host

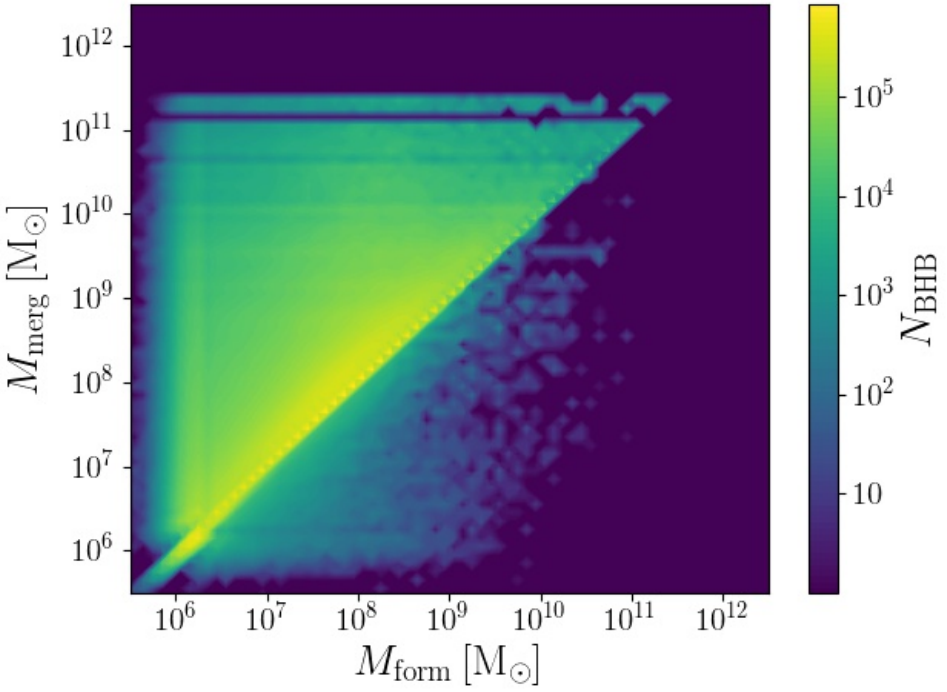

Figure 3.29: Plot showing the mass of the host where progenitor stars formed against the mass of the host where the BHBs merged at $z \sim 4$.

mass and progenitors metallicity. This effect, which has been already seen in the $z \sim 2$ case, is here enhanced. Considering even higher redshifts, so shorter delay times, we would find that the $M_{merg} - Z$ relation reproduces the $M_{form} - Z$ one, since we would consider those BHBs which would have formed and merged so quickly that host galaxies would have not undergone any effect from HC process.

3.4.2 NSBHs

The results of the analysis for NSBHs merged at $z \sim 4$ are similar to BHBs ones. From $M_{form} - M_{merg}$ correlation (Figure 3.32) we see that also NSBHs mergers mainly occurred in galaxies with mass equal or slightly higher that the formation one, principally in the range $10^7 - 10^{10}$ M$_\odot$. This is again due to the short time elapsed from the formation of the progenitors to the merger. Like BHBs, NSBHs merged at $z \sim 4$ formed at any time between $\sim$ 13.6 Gyr ago and $\sim$ 12.2 Gyr ago, with a preference for low t_{form}. As visible in Figure 3.33, it seems that NSBHs favour an even shorter delay time ($t_{delay} < 1$ Gyr) in addition to a little higher M_{form} than BHBs. Again, we do not see progenitors forming in $> 10^{11}$ M$_\odot$ galaxies since they are yet to be assembled.

The MZR's behaviour of NSBHs hosts resembles BHBs' one. The clear peak visible in the $z \sim 0.01$ case is here vanished and Illustris particles are more uniformly distributed across the MZR; moreover the spread in masses is lower than for the MZR found for NSBHs in more recent epochs. The metallicity range is unvaried, but again NSBHs progenitors can commonly have slightly higher Z compared to BHBs. Similar conclusions as for BHBs can be deducted from the $M_{merg} - Z$ plot in Figure 3.35: due to the short delay time we still partially see the MZR, with a concentration of mergers in the range $M_{merg} \sim 10^8 - 10^{10}$ M$_\odot$

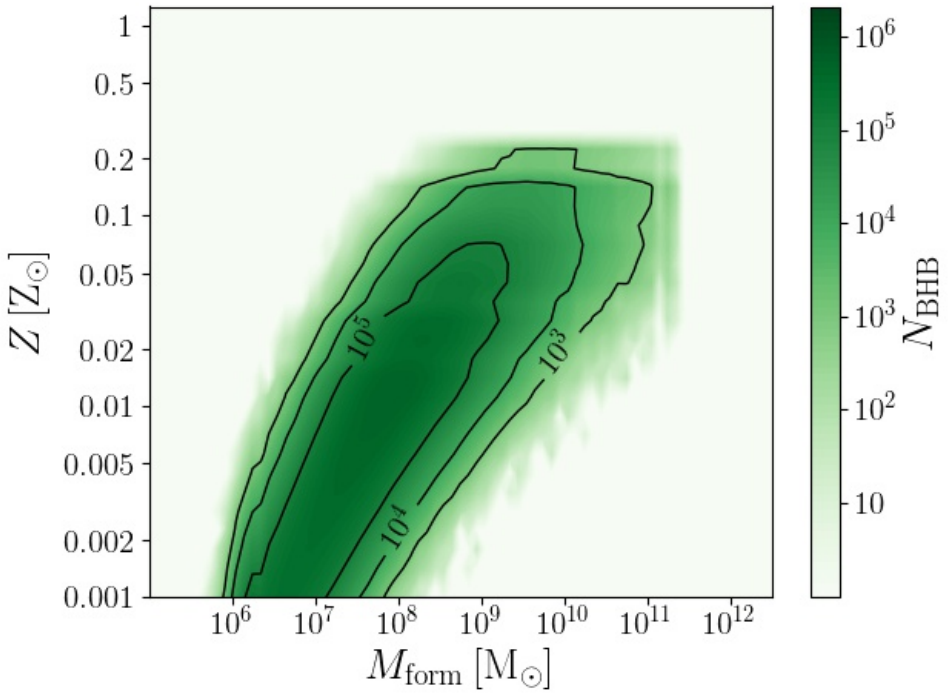

Figure 3.30: Plot showing the mass of the host where the progenitor stars of BHBs merged at $z \sim 4$ formed against their metallicity.

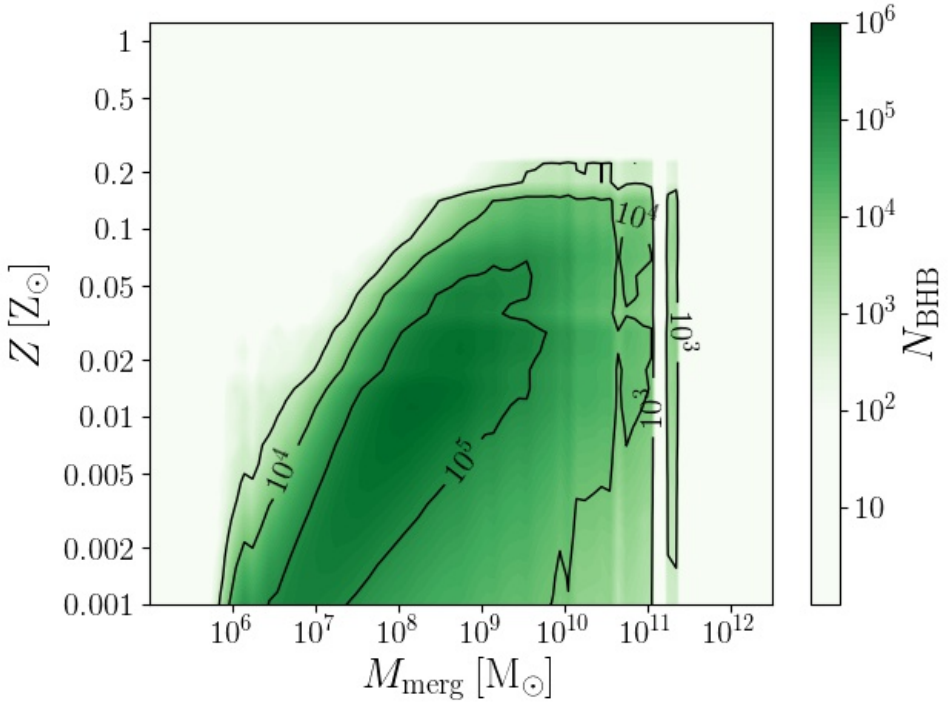

Figure 3.31: Plot showing the mass of the host where BHBs merged at $z \sim 4$ against progenitors' metallicity.

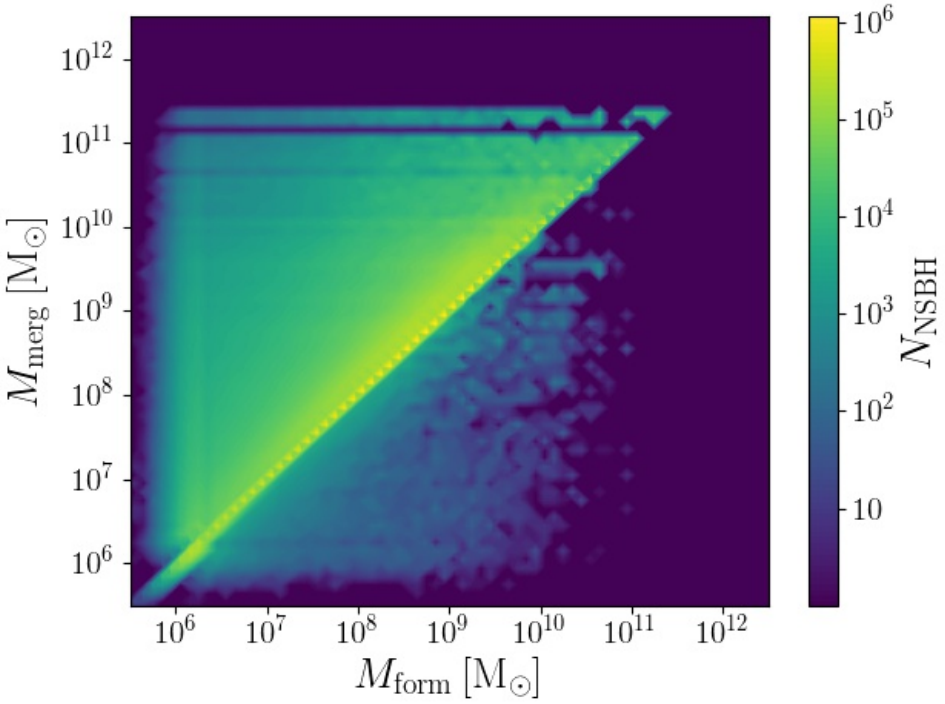

Figure 3.32: Plot showing the mass of the host where progenitor stars formed against the mass of the host where the NSBHs merged at $z \sim 4$.

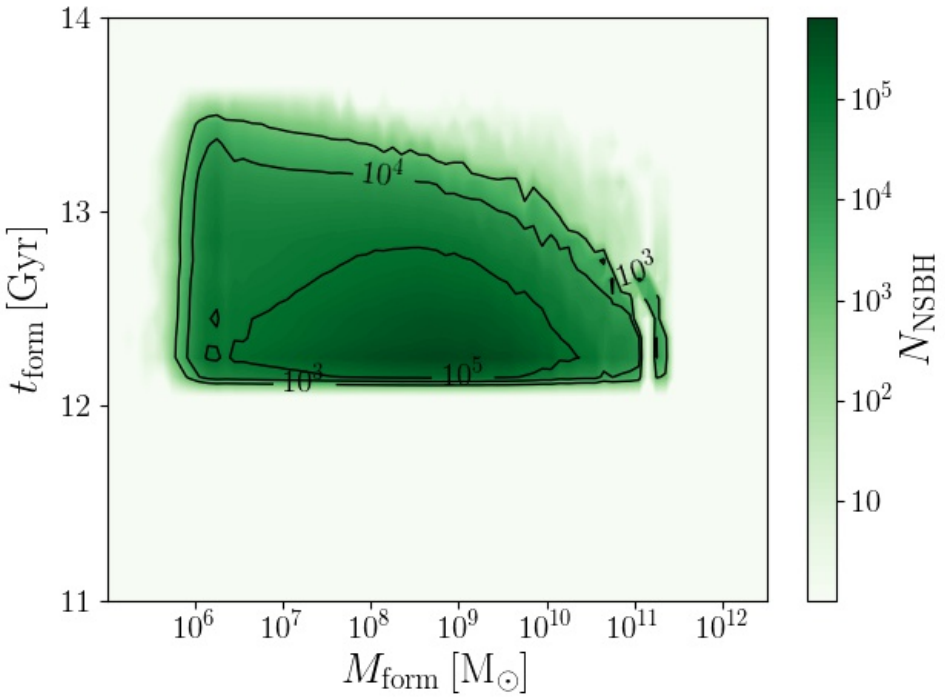

Figure 3.33: Mass of the formation host in function of the formation time of the progenitor stars of NSBHs which merged at $z \sim 4$.

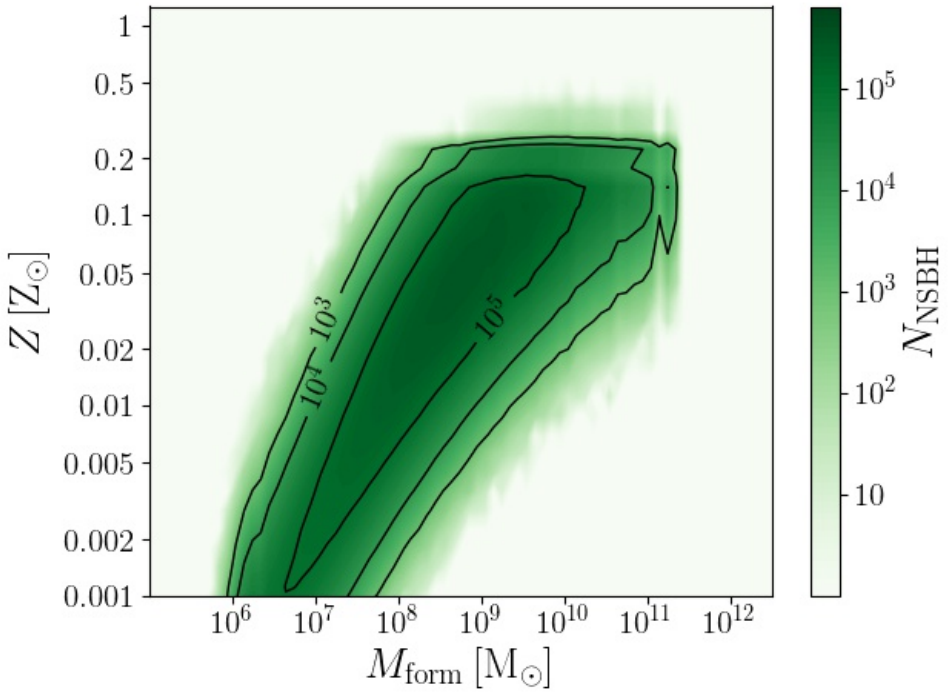

Figure 3.34: Plot showing the mass of the host where the progenitor stars of NSBHs merged at $z \sim 4$ formed against their metallicity.

and $Z \sim 0.005 - 0.2$ $\mathrm{Z}_\odot$. As in the previous cases, here we find merging NSBHs which had low-Z progenitors also in intermediate-mass and massive galaxies.

3.4.3 DNSs

Lastly we analyze the properties of DNSs merging at $z \sim 4$. As for BHBs and NSBHs which merged at $z \sim 4$, the delay time is short so in the plot $M_{form} - M_{merg}$ (Figure 3.36) we see that all mergers are located on the diagonal or slightly above it. While for the $z \sim 2$ and $z \sim 0.01$ cases we mainly found DNS mergers in massive galaxies, at $z \sim 4$ they are spread throughout the whole mass range $10^6 - 10^{11}$ $\mathrm{M}_\odot$. From Figure 3.37 we notice that the majority of progenitors formed $\lesssim 13$ Gyr ago; in particular it seems that the delay time for those mergers occurred in galaxies with masses $10^6 - 10^8$ $\mathrm{M}_\odot$ is of the order of ~ 0.7 Gyr while for those which occurred in more massive galaxies ($M_{form} \sim 10^9 - 10^{11}$ $\mathrm{M}_\odot$) it is even shorter, around $0.3 - 0.4$ Gyr.

We look for more information in the plot $M_{form} - Z$. Many metal-poor DNS progenitors form in low-mass galaxies: these are the ones which merged after a $t_{delay} \sim 0.7$ Gyr. Moreover, a lower number of mergers occurred in massive galaxies at high metallicities compared to the previous cases; these needed a very short t_{delay}, around $0.3 - 0.4$ Gyr. The maximum value for Z reached is here around ~ 5 $\mathrm{Z}_\odot$. We can again explain this trend considering that going back in time we increasingly find low-metallicity stars, but we should check about the validity of this correlation between t_{delay} and Z at high redshifts.

Finally, we analyze the $M_{merg} - Z$ relation (Figure 3.39). Again we notice that low-Z DNS progenitors can be found either in low-mass or massive galaxies at the merger epoch, while high-Z seems to merge in the same massive formation host, due to the extremely short

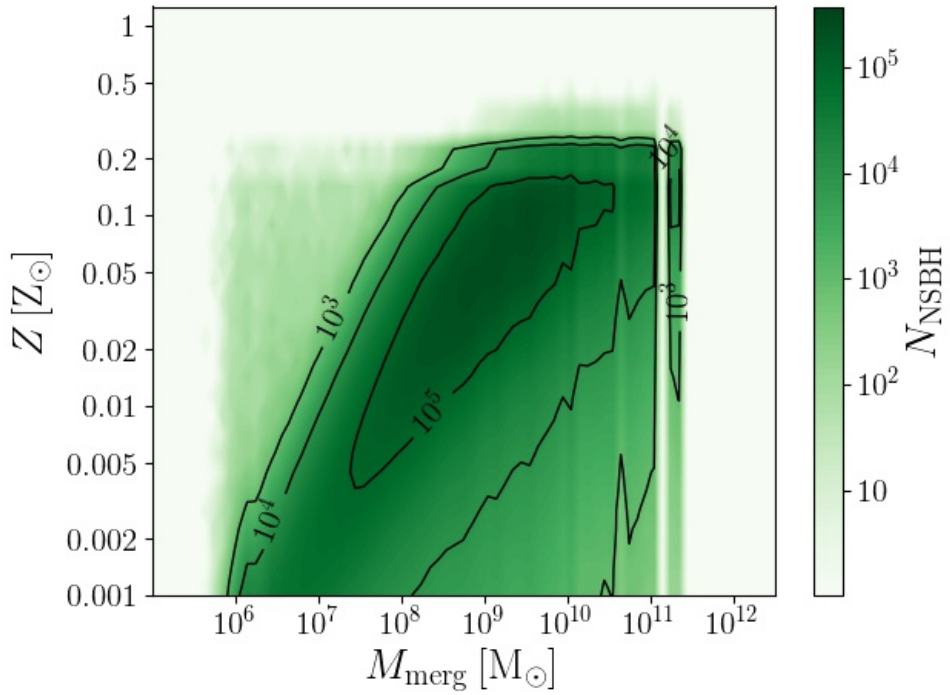

Figure 3.35: Plot showing the mass of the host where NSBHs merged at $z \sim 4$ against progenitors' metallicity.

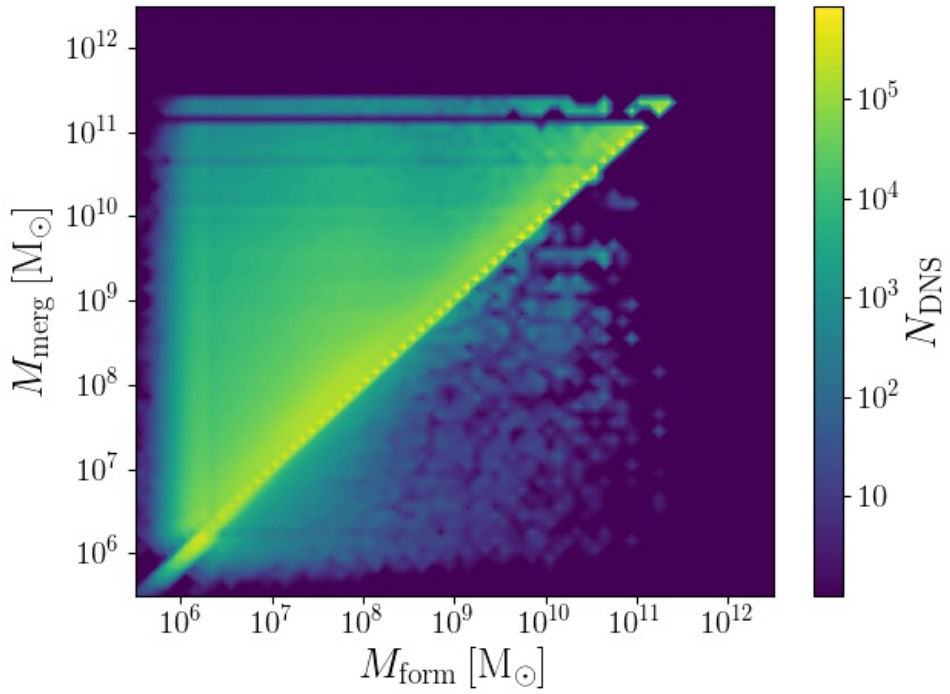

Figure 3.36: Plot showing the mass of the host where progenitor stars formed against the mass of the host where the DNSs merged at $z \sim 4$.

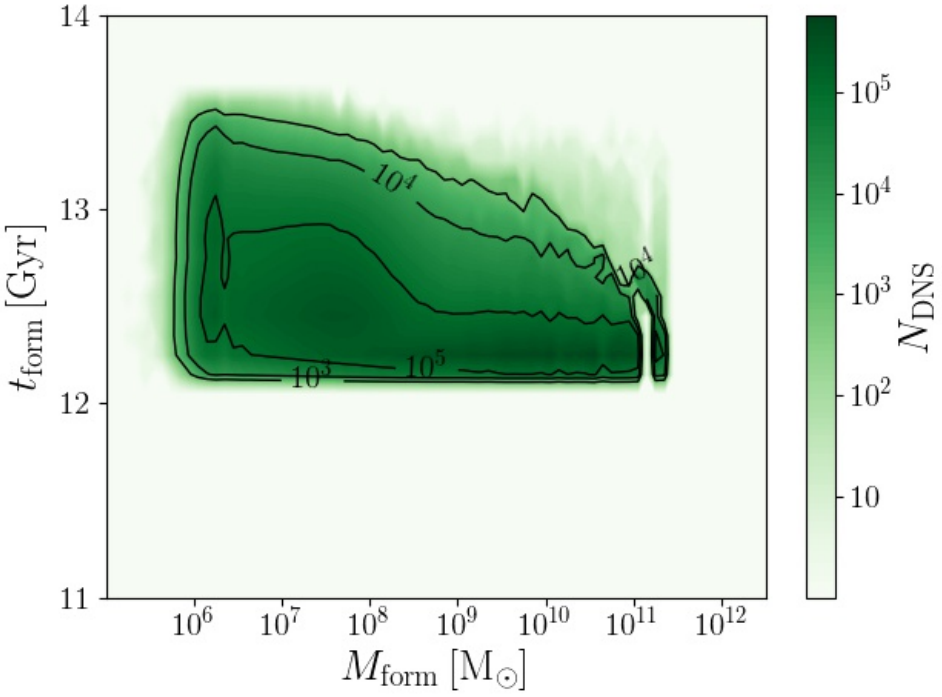

Figure 3.37: Mass of the formation host in function of the formation time of the progenitor stars of DNSs merged at $z \sim 4$.

delay time. The "critic" metallicity (Z_{crit}) at which this differentiation occurs is here around $0.01 - 0.02$ $Z_\odot$, thus similar to the $z \sim 2$ case and lower than in the $z \sim 0.01$ case. It seems there could be a sort of correlation between this Z_{crit} and the redshift. Following the trend, if we investigated higher redshifts, we would likely see less and less DNS progenitors with high metallicity, with a decreasing Z_{crit}. Bringing this argumentation to the extreme, we could have that Z_{crit} coincides with the progenitors' maximum Z at a certain high redshift, when all the stars have a very low metallicity.

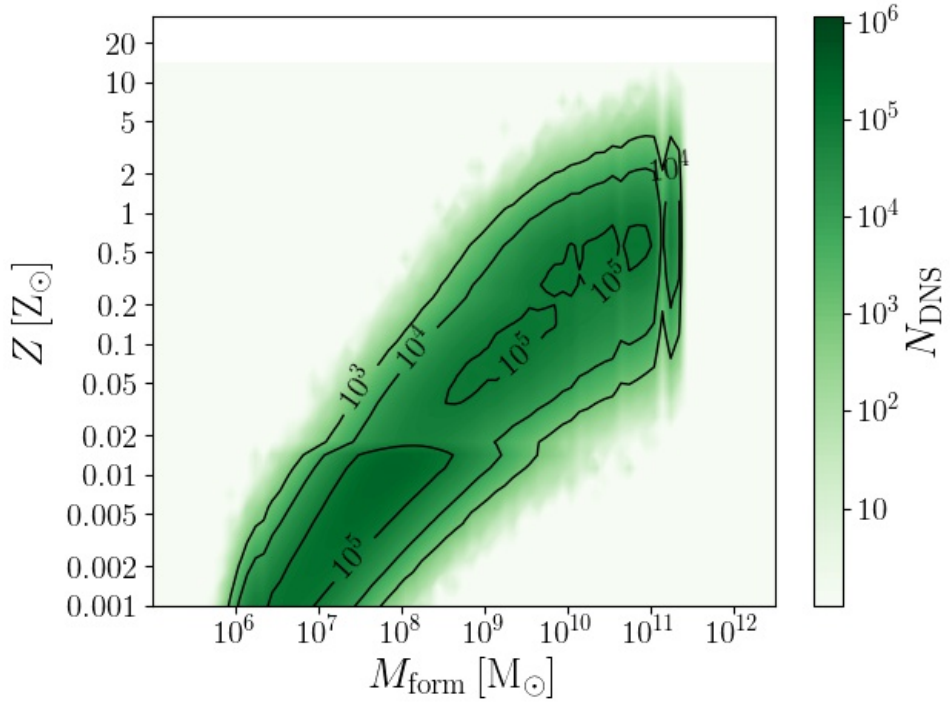

Figure 3.38: Plot showing the mass of the host where the progenitor stars of DNSs merged at $z \sim 4$ formed against their metallicity.

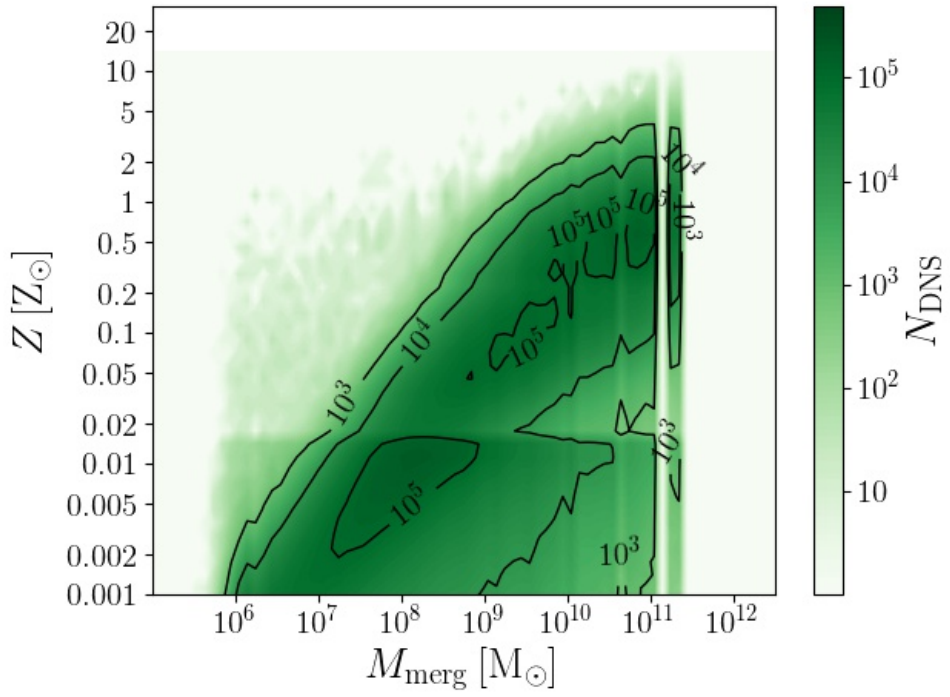

Figure 3.39: Plot showing the mass of the host where DNSs merged at $z \sim 4$ against progenitors' metallicity.

Chapter 4

Conclusions

In this work we have analyzed the properties of merging compact objects in relation to their environment, looking for possible correlations between the quantities of interest to us and how they may change across cosmic time. We have accomplished it combining the population-synthesis code MOBSE, which includes up-to-date prescriptions for stellar winds, pre-SN and SN phases, with the large-box Illustris cosmological simulation through a Monte Carlo approach. The masses and the merger rates of simulated compact objects are in agreement with the values inferred by LIGO-Virgo detections.

We summarize our final results for BHBs, NSBHs and DNSs in Sections 4.1, 4.2 and 4.3 respectively, followed by a brief description on how to carry on and improve this work in Section 4.4.

4.1 BHBs

We have seen that present-day merging BHBs mainly formed in a galaxy around 10 Gyr ago and merged in a more massive host galaxy after a long time, due to the HC build-up process. In general, BHBs need a longer delay time to reach the merger phase compared to the other analyzed compact objects, even at higher redshifts. The BHBs which merge nowadays have likely formed in galaxies with mass $10^7 - 10^9$ $M_\odot$ from low-metallicity progenitors, but they merge in galaxies of every mass in the range $10^7 - 10^{13}$ $M_\odot$; we expect to see a similar uniform distribution also for BHBs merging in dwarf galaxies (which are not resolved in the current simulation). We have seen that lower masses of the formation hosts and lower metallicities of BHB progenitors are more likely going back in time, because smaller galaxies and low-metallicity stars were more common. Moreover, we have seen how the merger rate for BHBs should increase by about a factor of 3 around $z \sim 2 - 3$, with a subsequent steep decrease going to less recent ages.

We show in Table 4.1 the main values for the quantities investigated above for BHB progenitors and their host galaxies at the various studied epochs.

4.2 NSBHs

NSBHs behave approximately as BHBs in every studied epoch. The NSBH progenitors formed in galaxies with masses comparable to BHBs hosts, from a range approximately $10^7 - 10^{11}$ $M_\odot$ at $z \sim 0.01$ down till $10^6 - 10^{9-10}$ $M_\odot$ at $z \sim 4$; for M_{merg} the trend is analogous: from approximately $10^8 - 10^{12}$ $M_\odot$ at $z \sim 0.01$ till $10^7 - 10^{10}$ $M_\odot$ at $z \sim 4$. In comparison, the formation times seem more peaked around certain values and the delay times a bit shorter than BHBs; moreover, NSBHs have a preference for a little higher values of Z at all epochs.

Table 4.1: Main values of the investigated properties of BHBs merging at different redshifts. Every estimate has been extracted from the plots and has then to be considered as an approximation.

	$z \sim 0.01$	$z \sim 2$	$z \sim 4$
M_{form} [$M_\odot$]	$10^7 - 10^9$	$10^7 - 10^9$	$10^6 - 10^9$
M_{merg} [$M_\odot$]	$10^7 - 10^{13}$	$10^7 - 10^{11-12}$	$10^6 - 10^9$
Z [$Z_\odot$]	$0.05 - 0.1$	$0.001 - 0.2$	$0.001 - 0.05$
t_{form} [Gyr]	$8 - 13$	$10.5 - 13$	$12.3 - 13.1$
t_{delay} [Gyr]	10	$2 - 2.5$	1

Table 4.2: Main values of the investigated properties of NSBHs merging at different redshifts. Every estimate has been extracted from the plots and has then to be considered as an approximation.

	$z \sim 0.01$	$z \sim 2$	$z \sim 4$
M_{form} [$M_\odot$]	$10^7 - 10^{11}$	$10^7 - 10^{10}$	$10^6 - 10^{9-10}$
M_{merg} [$M_\odot$]	$10^8 - 10^{12}$	$10^8 - 10^{11}$	$10^7 - 10^{10}$
Z [$Z_\odot$]	$0.05 - 0.2$	$0.002 - 0.2$	$0.001 - 0.2$
t_{form} [Gyr]	$10 - 12$	$10.4 - 12.2$	$12.2 - 12.9$
t_{delay} [Gyr]	10	2	< 1

It seems there is a sort of correlation between the short delay time and the high metallicity of progenitors. We foresee an increase of the merger rate of about a factor of 10 at redshifts $1.5 - 3$, followed by a rapid decrease for the farthest epochs.

The main values of the analyzed quantities at different redshifts for NSBHs are visible in Table 4.2.

4.3 DNSs

Our results for DNSs show a preference for a different environment, compared to BHBs and NSBHs. Typical delay times are very short already at $z \sim 0.01$ and become even shorter at higher redshifts, from $\lesssim 2$ Gyr to less than 1 Gyr. In particular, we see at $z \sim 4$ that there could be a correlation between t_{delay} and the mass of the host galaxy where the progenitors form: we obtained a little shorter delay times for galaxies more massive than 10^{8-9} $M_\odot$. A direct implication for a short t_{delay} is that the mass of the formation host and the mass of the galaxy where the merger occurred could not be substantially different, due to the long timescale needed by massive galaxies to build-up; likely the merger took place in the same host where the progenitors had formed. We found that the mass range $10^9 - 10^{11}$ $M_\odot$, in which we foresee to find the vast majority of DNSs nowadays, is consistent with the mass range found for short gamma-ray burst hosts.

DNS progenitors have a strong predisposition for very high metallicity at any epochs, till many times the solar one. We notice that the distribution of metallicities for DNSs at the present day is bimodal, with a small peak at low Z and a major one at high Z. Moreover, we found that at any epoch DNSs with high-Z progenitors are the ones which reached the

Table 4.3: Main values of the investigated properties of DNSs merging at different redshifts. Every estimate has been extracted from the plots and has then to be considered as an approximation.

	$z \sim 0.01$	$z \sim 2$	$z \sim 4$
M_{form} [$M_\odot$]	$10^9 - 10^{11}$	$10^7 - 10^{12}$	$10^{6-7} - 10^{11}$
M_{merg} [$M_\odot$]	$10^9 - 10^{11}$	$10^7 - 10^{12}$	$10^{6-7} - 10^{11}$
Z [$Z_\odot$]	$0.2 - 5$	$0.01 - 0.02$ - $0.05 - 5$	$0.001 - 1$
t_{form} [Gyr]	< 2	$10.4 - 11.8$	$12.2 - 13$
t_{delay} [Gyr]	< 2	< 1.5	< 0.7
Z_{crit} [$Z_\odot$]	$0.05 - 0.1$	0.02	$0.01 - 0.02$

merger phase in a shorter time, while low-Z ones needed a longer delay time. This effect is more and more visible with increasing redshift. Since at high redshifts we find more low-Z stars, the first peak in the metallicity distribution of DNSs becomes more populated, while the opposite occurs for the second peak; in addition, the maximum Z of DNS progenitors decreases. The differentiation between these 2 trends occurs at a certain metallicity, named Z_{crit}, which decreases from a value around $0.05 - 0.1$ $Z_\odot$ at the present day to about 0.02 $Z_\odot$ at high z. So what we have found is that for DNSs there is a clear correlation between t_{delay}, Z and M_{form} visible at any epoch: a short delay time is related to high-Z progenitors forming in massive galaxies and vice versa. These quantities scale with the redshift. We found a similar relation $t_{delay} - Z$ for NSBHs, but in comparison it is weaker. In addition, a $Z_{crit} - z$ correlation could exist for DNSs. Last but not least, we foresee an increase in the merger rate for DNSs of about a factor of $3 - 4$ at $z \sim 1 - 2$.

The main values of the analyzed properties of DNS progenitors and hosts at redshifts $z \sim 0.01$, 2 and 4 are shown in Table 4.3.

4.4 What else?

With this work we have found crucial properties for progenitors and host galaxies of merging compact objects, but we can still improve. Firstly, we can perform the analyzes for an higher number of redshifts, to obtain a clearer view of how the investigated properties evolve along with redshift, paying particular attention to the correlations between t_{delay}, Z and M_{form} found for DNSs and checking the validity and the meaning of the $Z_{crit} - z$ relation. Secondly, we can flank the Illustris with a small-box high-resolution simulation: in such way we will be able to reproduce and study compact objects merging in dwarf galaxies.

An interesting complementary future work may be extending the range of the investigated properties for host galaxies, analyzing their possible belonging to a galaxy cluster and their morphological type, in order to create a complete tool with which is possible to support LIGO search for the host of a GW-emitting event if the electromagnetic counterpart is not available.

References

[1] Acernese, F. et al. "Advanced Virgo: a second-generation interferometric gravitational wave detector". In: *Classical and Quantum Gravity, 32, 2* (2015).

[2] B., Downing J. M. et al. In: *Monthly Notices of the Royal Astronomical Society, 416, 133* (2011).

[3] Belczynski, K. et al. In: *The Astrophysical Journal, 714, 2* (2010).

[4] Berger, E. In: *Annual Review of Astronomy and Astrophysics* (2014).

[5] Bird, S. et al. In: *Physical Review Letters, 116, 201301* (2016).

[6] Broadhurst, T., Diego, J. M., and Smoot, G. 2018. arXiv: `1802.05273 [astro-ph.CO]`.

[7] Carr, B. et al. In: *Physical Review Documents, 94, 083504* (2016).

[8] Chen, Y. et al. In: *Monthly Notices of the Royal Astronomical Society, 452, 1068* (2015).

[9] de Jager, C., Nieuwenhuijzen, H., and van der Hucht, K. A. In: *Astronomy & Astrophysics Supplement Series, 72, 2* (1988).

[10] Ertl, T. et al. In: *The Astrophysical Journal, 818, 2* (2016).

[11] Farr, W. M. et al. In: *The Astrophysical Journal, 741, 2* (2011).

[12] Farr, W. M. et al. In: *Nature, 548* (2016).

[13] Fryer, C. L., Belczynski, K., Wiktorowicz, G., et al. In: *The Astrophysical Journal, 749, 91* (2012).

[14] Genel, S. In: *Monthly Notices of the Royal Astronomical Society, 822, 2* (2016).

[15] Genel, S. et al. In: *Monthly Notices of the Royal Astronomical Society, 445, 1* (2014).

[16] Gerosa, D. and Berti, E. In: *Physical Review Documents, 95, 124046* (2017).

[17] Giacobbo, N. "Un nuovo codice di sintesi di popolazione per lo studio della demografia di binarie di buchi neri". MA thesis. Università di Padova, 2016.

[18] Giacobbo, N. and Mapelli, M. 2018. arXiv: `1805.11100 [astro-ph.SR]`.

[19] Giacobbo, N., Mapelli, M., and Spera, M. In: *Monthly Notices of the Royal Astronomical Society, 474, 3* (2018).

[20] Giacobbo, N. et al. 2018. arXiv: `1711.03556 [astro-ph.SR]`.

[21] Gräfener, G. and Hamann, W.-R. In: *Astronomy & Astrophysics, 432, 2* (2008).

[22] Hall, P. D. and Tout, C. A. In: *Monthly Notices of the Royal Astronomical Society, 444, 4* (2014).

[23] Hinshaw, G. et al. In: *The Astrophysical Journal Supplement, 208, 2* (2013).

[24] Hobbs, G. et al. In: *Monthly Notices of the Royal Astronomical Society, 360, 3* (2005).

[25] Hurley, J. R., Tout, C. A., and Pols, O. R. In: *Monthly Notices of the Royal Astronomical Society, 329, 4* (2002).

[26] Inomata, K. et al. In: *Physical Review Documents, 95, 123510* (2017).

[27] Lamberts, A. et al. In: *Monthly Notices of the Royal Astronomical Society: Letters, 463, 1* (2016).

[28] Leibler, C. N. and Berger, E. In: *The Astrophysical Journal, 725, 1* (2010).

[29] Madau, P. and Dickinson, M. In: *Annual Review of Astronomy and Astrophysics, 52* (2014).

[30] Magee, R. and Hanna, C. 2017. arXiv: `1706.04947 [astro-ph.CO]`.

[31] Maiolino, R. et al. In: *Astronomy & Astrophysics, 488, 2* (2008).

[32] Mapelli, M. and Giacobbo, N. 2018. arXiv: `1806.04866 [astro-ph.HE]`.

[33] Mapelli, M., Giacobbo, N., Toffano, M., et al. In: (2018). arXiv: `1809.03521 [astro-ph.HE]`.

[34] Mapelli, M. et al. In: *Monthly Notices of the Royal Astronomical Society, 429, 3* (2013).

[35] Mapelli, M. et al. 2017. arXiv: `1708.05722 [astro-ph.GA]`.

[36] Neistein, E., van den Bosch, F. C., and Dekel, A. In: *Monthly Notices of the Royal Astronomical Society, 372, 2* (2006).

[37] O'Connor, E. and Ott, C. D. In: *The Astrophysical Journal, 730, 70* (2011).

[38] Ohlmann, S. T. et al. In: *The Astrophysical Journal Letter, 816, L9* (2016).

[39] Özel, F. et al. In: *The Astrophysical Journal, 725, 1918* (2010).

[40] Passy, J. C. et al. In: *The Astrophysical Journal, 744, 52* (2012).

[41] Ricker, P. M. and Taam, R. E. In: *The Astrophysical Journal Letter, 672, L41* (2008).

[42] Ricker, P. M. and Taam, R. E. In: *The Astrophysical Journal, 746, 74* (2012).

[43] Spera, M. and Mapelli, M. In: *Monthly Notices of the Royal Astronomical Society, 470, 4* (2017).

[44] Spera, M., Mapelli, M., and Bressan, A. In: *Monthly Notices of the Royal Astronomical Society, 451, 4* (2015).

[45] The LIGO Scientific Collaboration, Aasi, J., et al. "Advanced LIGO". In: *Classical and Quantum Gravity, 32, 7* (2015).

[46] The LIGO Scientific Collaboration, Abbott, B. P., et al. In: *Physical Review Letters 116, 061102* (2016).

[47] The LIGO Scientific Collaboration, Abbott, B. P., et al. In: *Physical Review Letters 116, 241102* (2016).

[48] The LIGO Scientific Collaboration, Abbott, B. P., et al. In: *The Astrophysical Journal Letters, 833, 1* (2016).

[49] The LIGO Scientific Collaboration, Abbott, B. P., et al. In: *The Astrophysical Journal Letters, 818, L22* (2016).

[50] The LIGO Scientific Collaboration, Abbott, B. P., et al. In: *Physical Review Letters 119, 161101* (2017).

[51] Troya, E. et al. In: *The Astrophysical Journal, 827, 2* (2016).

[52] Vink, J. S. and de Koter, A. In: *Astronomy & Astrophysics, 442, 2* (2005).

[53] Vink, J. S., de Koter, A., and Lamers, H. J. G. L. M. In: *Astronomy & Astrophysics, 369, 2* (2001).

[54] Vogelsberger, M. et al. 2014. arXiv: `1405.2921 [astro-ph]`.

[55] Woosley, S. E., Heger, A., and Weaver, T. A. In: *Reviews of Modern Physics, 74, 1015* (2002).

[56] Ziosi, B. M. et al. In: *Monthly Notices of the Royal Astronomical Society, 441, 4* (2014).